Regulating d-orbital hybridization of subgroup-IVB single atoms for efficient oxygen reduction reaction.

ZHAO, X., SUN, Y., WANG, J., NIE, A., ZOU, G., REN, L., WANG, J., WANG, Y., FERNANDEZ, C. and PENG, Q.

2024

Regulating *d*-Orbital Hybridization of Subgroup-IVB Single Atoms for Efficient Oxygen Reduction Reaction

Xue Zhao [a], Yong Sun [a], Jinming Wang [a], Anmin Nie [a], Guodong Zou [a],* Liqun Ren [b], Jing Wang [a], Yong Wang [c], Carlos Fernandez [d], and Qiuming Peng [a]*

a State Key Laboratory of Metastable Materials Science and Technology Yanshan University, Qinhuangdao 066004, P. R. China
E-mail: zouguodong@ysu.edu.cn; pengqiuming@ysu.edu.cn

b Laboratory of Spinal Cord Injury and Rehabilitation, Chengde Medical University, Chengde 067000, P. R. China

c College of Chinese Medicine, Beijing University of Chinese Medicine Beijing 100029, P. R. China

d School of Pharmacy and life sciences, Robert Gordon University, Aberdeen AB107GJ, UK

ABSTRACT:
Highly active single-atom electrocatalysts for the oxygen reduction reaction are crucial for improving the energy conversion efficiency, but they suffer from a limited choice of metal centers and unsatisfactory stabilities. Here, this work reports that optimization of the binding energies for reaction intermediates by tuning the *d*-orbital hybridization with axial groups converts inactive subgroup-IVB (Ti, Zr, Hf) moieties (MN_4) into active motifs (MN_4O), as confirmed with theoretical calculations. The competition between metal-ligand covalency and metal-intermediate covalency affects the *d-p* orbital hybridization between the metal site and the intermediates, converting the metal centers into active sites. Subsequently, dispersed single-atom M sites coordinated by nitrogen/oxygen groups have been prepared on graphene (s-M-N/O-C) catalysts on a large-scale with high-energy milling and pyrolysis. Impressively, the s-Hf-N/O-C catalyst with 5.08 wt% Hf exhibits a half-wave potential of 0.920 V and encouraging performance in a zinc-air battery with an extraordinary cycling life of over 1600 h and a large peak power-density of 256.9 mW cm^{-2}. This work provides promising single-atom electrocatalysts and principles for preparing other catalysts for the oxygen reduction reaction.

1. Introduction

Electrochemical energy conversion plays an important role in meeting energy demand and eliminating environmental pollution, which is attributed to the achievement of dual-carbon targets.[1] Efficient electrocatalysts are essential for energy conversion, such as fuel cells and metal-air batteries.[2] These catalysts minimize the over potential for the heterogeneous oxygen reduction reaction (ORR) and directly convert O_2 to OH− in an alkaline medium via a four-electron route.[3] Currently, platinum-group metal(PGM) materials are the state-of-art catalysts for the ORR. However, they are plagued by low crustal abundances, high costs, and inferior durabilities.[4] Thus, bioinspired single-atom M-N-C (M=Fe,Co, Ni, Mn) catalysts (SACs) composed of individual metals embedded in nitrogen-doped carbon substrates show promise in replacing PGMs.[5] These SACs show attractive features, such as various coordination configurations, multiple reaction environments, and good catalytic activities. In these systems, Fe-N-C provides high ORR activity, but it also degrades quickly because Fe^{2+} ions enable side reactions.[6] Co-N-C improves the stability at the expense of selectivity.[7] The ORR activities of Mn-N-C or Ni-N-C are inferior to those of Fe-N-C and Co-N-C,[8] so fabricating competent and modified MN_x motifs with suitable elements is important but challenging. According to the d-band center model proposed by Hammer and Nørskov, the proper adsorption strength, neither too strong nor too weak, is required to prepare for the highly active catalyst.[9] In principle, the key reason for poor MN_4 motifs is the sluggish ad/desorption processes of intermediates based on weak/strong binding with metals. On this basis, two routes have been used to adjust these reactions in the last decade. One involves metal-to-metal interactions, such as bimetallic or/and multiple-metallic catalysts, which exhibit high reactivity by adjusting the charge distribution among different metal centers.[10] The other is the direct regulation of the metal cores with highly electronegative ligands, such as O, S or F, resulting in the formation of various coordination configurations.[11] Both of these approaches involve the metal cores. As a result, the appropriate metal elements play a key role in designing effective ORR catalysts. Compared with other transition metals, the subgroup-IVB elements (Ti, Zr, and Hf) have necessary characteristics to develop highly efficient ORR catalysts, including low costs. There are five d-orbitals (d_{xy}, d_{yz}, d_{xz}, d_{z^2}, $d_{x^2-y^2}$), which provide enough opportunities to accept electrons during the ORR process and enable efficient O_2 adsorption and activation.[12] Of course, this strong

binding also inhibits desorption of the reaction intermediates.[13] Consequently, the development of highly active subgroup-IVB metal cores requires weakening the adsorption strength of the reaction intermediates. Theoretically, each subgroup-IVB metal core can bind six nearest N neighbors in bulk MN,[14] en-abling the preparation of six-ligand complexes. Nevertheless, the fabrication of six N-based motifs might be restricted by the spatial orientations in a two-dimensional material. Therefore, modification of the axial substituents in d-orbital hybridization could alter the bonding strength by regulating the charge den-sity of the metal site.[15] Specifically, unlike N ligands, the ax-ial O ligands have more electrons to occupy more external orbitals. Thus, it is possible to form stable catalytic motifs with spatially limited two-dimensional substrates by reducing the coordination number. More importantly, the axial oxygen ligand could weaken the adsorption of the reaction intermediates with its larger atomic radius and serve as a "spatial fence" to avoid the formation of metal clusters during high-temperature pyrolysis.

In this work, we use density function theory (DFT) calcula-tions to show that the inactive subgroup-IVB (Ti, Zr, and Hf) moieties (MN_4) can be activated as MN_4O active sites by regulating the d-orbital hybridization with an axial oxygen ligand. Inspired by the theoretical predictions, we synthesized dual-ligand confining single-atomic MN_4O moieties (with four coplanar Ns and one out-of-plane O ligands moiety) by an industrial milling and pyrolysis, and the motif was characterized with a series of analytical techniques. We assessed their electrocatalytic activities and battery performance. Attractively, the s-Hf-N/O-C catalyst with 5.08 wt % Hf showed high electrocatalytic activity and good cycling stability, as confirmed with Zn-air batteries. This axial-group modification strategy with subgroup-IVB metals proved to be effective in developing new M-N-C SACs and might be extended to other subgroups.

2. Results and Discussion

2.1. Theoretical Analysis

To explore the effect of the axial oxygen ligand on the local coordination geometry and electron configuration of the subgroup-IVB complexes, two MN_4 and MN_4O structural models were established for the DFT calculations. The geometries for the M-N bonds in the MN_4O were remarkably different from those of MN_4, signifying geometrical structure distortion of MN_4O (Table S1, Supporting Information). As evidenced by the den-sity of states (DOS), the axial-oxygen ligand resulted in occupation of d-orbitals on the M center of MN_4O, causing the typical diamagnetism. Evidently, partial electron transfer occurred from the M to N and/or O center and redistributed the electron density (Figure S1, Supporting Information). As shown in Figure S2 (Supporting Information), the yellow isosurface corresponds to the electron depletion region and the blue one represents the electron increase zone. Compared with the MN_4, the difference in charge density between the M core and ligands was obviously reduced in MN_4O due to the presence of the axial oxygen ligand. The local electron configuration was examined through projected density of states (PDOS) calculations (**Figures** 1a,b and S3,S4, Supporting Information). The PDOS for the d-orbitals in MN_4 revealed an asymmetrical arrangement. Conversely, the PDOS for the d-orbitals of M were restructured, and the electrons in the d-orbitals provided a symmetrical arrangement of the MN_4O group.

To investigate the effect of axial oxygen on the ORR reaction, we determined the adsorption strength between the metal active site and intermediates by calculating the Mayer bond order of each intermediate with HfN_4 and HfN_4O (Figure 1c). The Mayer bond order was defined by the density matrix P and the overlapping matrix S, which also was an useful tool for chemical bonding analysis.[16] The ORR began with *OOH (the first ORR intermediate) occupying the catalytic site, and the entire ORR cycle finished as soon as *OH (the final ORR intermediate) was released. Due to orbital interactions, HfN_4O exhibits a higher strength of *OOH adsorption (1.12) compared to HfN_4 (1.03) in favor of the start of ORR. Meanwhile, the bond order of *OH on HfN O was 1.27, which was lower than that of HfN_4 (1.37). This indicated a weaker orbital interaction between the metal core and reaction intermediate for HfN_4O, which improved the ORR activity in terms of the release of the *OH based on thermodynamics.[17]

In addition, we also calculated the projected crystal orbital Hamilton populations (pCOHP) between the Hf atom and the O atom of *OH to explain the bond strength (Figure 1d,e). For HfN_4 and HfN_4O, the main components of the Hf-O interactions are attributed to the contributions of the $d_z^2\text{-}p_z$, $d_{xz}\text{-}p_x$ and $d_{yz}\text{-}p_y$ orbitals.[18] Therefore, we focused on the different bonding states of the $d_z^2\text{-}p_z$, $d_{xz}\text{-}p_x$ and $d_{yz}\text{-}p_y$ orbitals of HfN_4 and HfN_4O by pCOHP analysis. As shown in Figure 1d,e, the σ-orbital peaks of the HfN_4O model are significantly lower compared with those of the HfN_4 model, which proves that the Hf $5d_z^2$-O $2p_z$ orbitals have weaker interactions, weakening the Hf-O bond strength.[19] Additionally, the more positive integral COHP (ICOHP) value for Hf-O bonding to reach the Fermi energy level for HfN_4O also confirms weaker OH coupling.[17b] It demonstrates that axial O coordination modulates the $Hf_4\,5d_z^2$ orbitals, and optimizes the adsorption strength of the HfN_4O active center to OH intermediates, enhancing its oxygen reduction activity.

To probe the ORR catalytic activities of different moieties, the reaction free energy of each ORR elementary step of MN_4 and reaction free energy of each ORR elementary step of MN_4 and MN_4O was calculated based on an associative mechanism (Figure S5, Supporting Information).[20] As shown in the free energy diagram at 0 V (Figure 1f), strong binding of *OH in the last reaction step (*OH→H_2O) is an uphill process with the MN_4 models, which is a potential rate-determining step (RDS). In contrast, the MN_4O model with axial oxygen coordination showed a lower adsorption energy for *OH, so the RDS was clearly changed by

addition of the axial oxygen ligand. The formation of *OOH ($O_2 \rightarrow$ *OOH) was the RDS in the ORR process with HfN$_4$O. Over the entire ORR process, there was no evidence of steric repulsion between the axial oxygen ligand and intermediate, indicating that HfN$_4$O adopted a favorable geometric configuration (Figure S6, Supporting Information). Additionally, FeN$_4$, NiN$_4$, MnN$_4$, and commercial Pt/C were used to seek trends. In the volcanic diagram, the TiN$_4$, ZrN$_4$, and HfN$_4$ sites showed severe ORR overpotentials, indicating endothermic reactions. Comparatively, the tailored *d*-orbital splitting endowed MN$_4$O with a very low overpotential. In particular, the pentacoordinate configuration of the HfN$_4$O moiety was at the top of the volcano plot, which was lower than those of Pt/C and other models (Figure 1g).[21]

To evaluate the catalytic performance, the adsorption energies of the key reaction intermediates were determined. Figure 1h shows a plot of the volcano map as a function of ΔG_{*OH} and ΔG_{*OOH}, in which all MN catalysts were linearly located at the lower left side of the volcano map where ΔG_{*OH} was less than 0.5 eV. This demonstrated that the strong binding of OH* severely hampered the ORR process, and the host levels of most metal sites were not suitable.[22] Due to the introduction of the O atoms, the adsorption of reaction intermediates varied, and the points moved to near the blue triangle region. The data point for the HfN$_4$O model was located near the top of the volcano map, consistent with the volcano plot. Additionally, the lower formation energy for the MN$_4$O (M = Ti, Zr, Hf) relative to that of MN$_4$ indicated that the pentacoordinate structure was more energetically favorable than the tetracoordinate structure (Figure 1i). Note that the low formation energy for MN$_4$O reflected the excellent chemical stability of the pentacoordinated catalyst, which effectively inhibited the local structure collapse of metal sites during the ORR process. Consequently, the decreased polarization of the d_{xz}, d_{yz}, and $d_z{}^2$ orbitals caused by the changing *d*-orbital configuration enables a favorable binding strength of *OH.

2.2. Syntheses and Characteristics of Single-Atom Hf Sites

The straightforward two-step high-energy milling and pyrolysis process, shown in **Figure 2a** was used to prepare dispersed single-atom Hf sites coordinated by nitrogen/oxygen on graphene (labelled s-Hf-N/O-C) catalysts. Basically, the characteristic X-ray diffraction (XRD) peaks for HfCl$_4$ or Hf metal were not detected after ball milling of the product, which proved that all Hf atoms reduced by Mg were homogenously dissolved in the Mg matrix, as shown by the left-shifted peaks for Mg in the XRD patterns (Figure S7, Supporting Information). Additionally, excess Cl atoms were released as Cl$_2$.[23] Afterwards, the milled powders were calcined in a tube furnace under 900 °C in a mixed (1:1) atmosphere of CO$_2$ and NH$_3$; carbon skeleton collapse was not observed, high reactivity was maintained. Thus, the Mg matrix was transferred into MgO and graphene during pyrolysis under CO$_2$, and some Hf atoms were converted into HfO$_2$ due to their high oxygen affinity.[24] Ammonia was the source of the N, and defects and/or vacancies were formed on the graphene substrate during pyrolysis; these served as good anchoring sites or directly encapsulated the atomically dispersed Hf on the N/O-doped graphene. Finally, HfN$_4$O motifs were prepared on the N/O-doped graphene (Figure 2b) after removing the free-standing oxide residues with HF acid picking. The reaction process can be summarized as follows:

$$HfCl_4 + Mg \rightarrow MgHf + Cl_2 \qquad\qquad (1)$$

$$MgHf + CO_2 + NH_3 \rightarrow MgO + \left(Hf + Hf\,O_2\right) - N/O - C + H_2O \qquad (2)$$
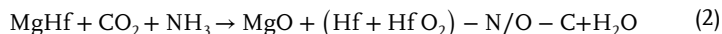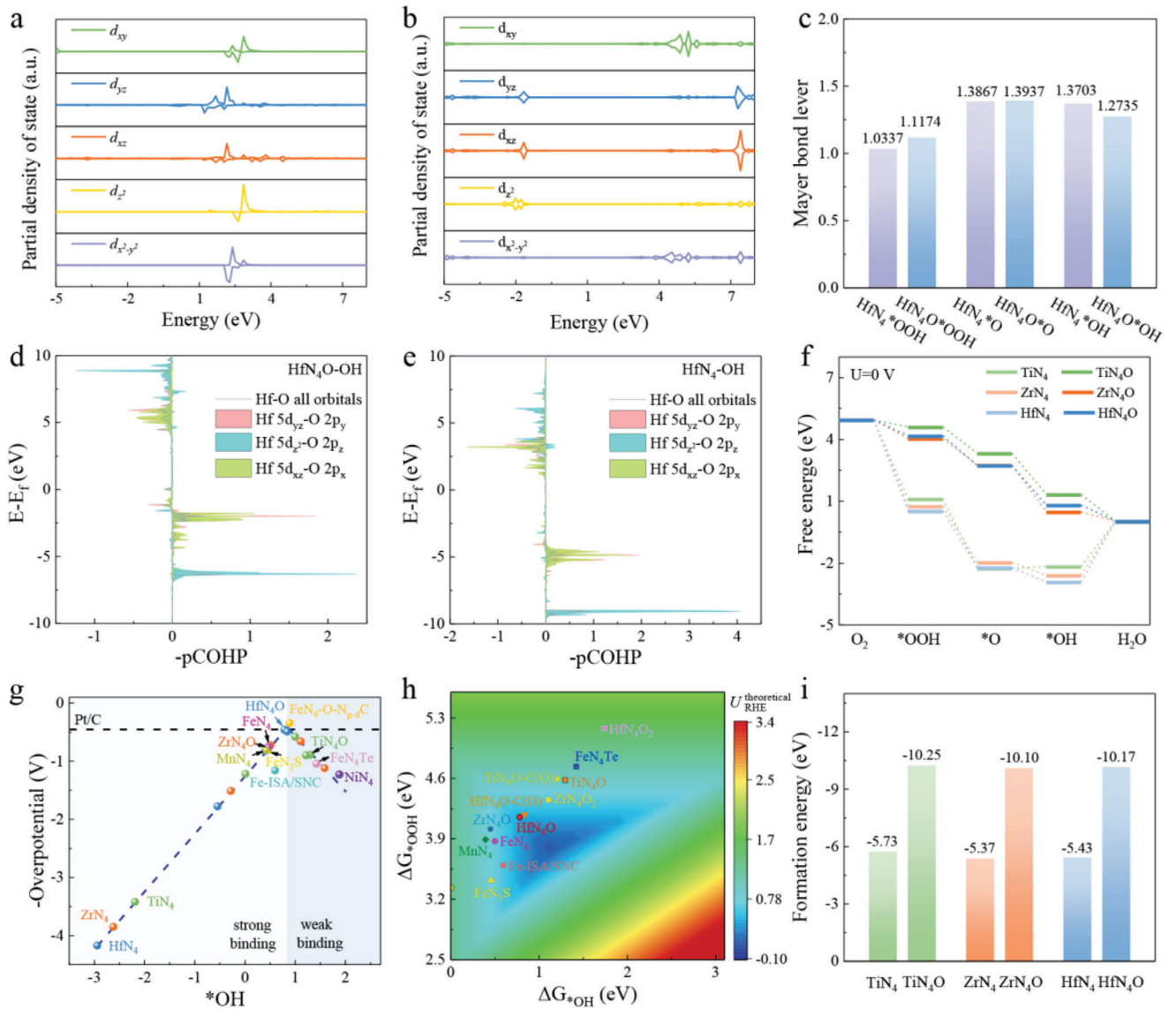
Figure 1. Theoretical calculations. a,b) Projected density of states (PDOS) on *d* orbital of Hf for HfN$_4$ and HfN$_4$O models. c) The Mayer bond levels between HfN$_4$ and HfN$_4$O models and intermediates. d,e) Projected crystal orbital Hamilton populations (pCOHP) between Hf and p-orbital of O of *OH on HfN$_4$ and HfN$_4$O models. f) Theoretical oxygen reduction reaction (ORR) overpotential of subgroup-IVB moieties calculated from the Gibbs free energy diagram. g) Calculated catalytic activity volcano plots. h) Color-filled contour plots of the activity as the function of both $\triangle$G$_{*OOH}$ and $\triangle$G$_{*OH}$. i) The formation energy diagrams for different subgroup-IVB moieties.
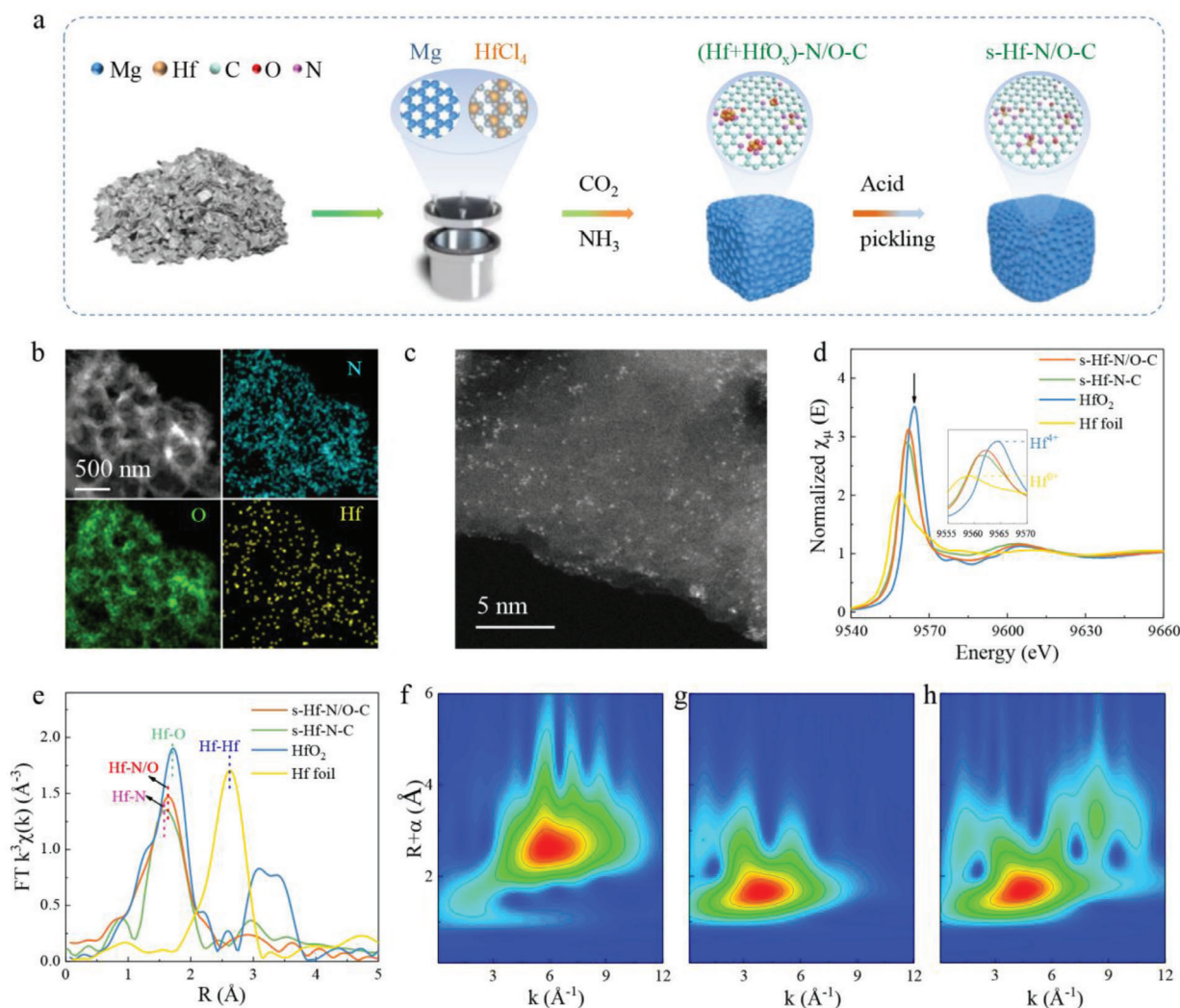
Figure 2. Synthesis and characterization of the s-Hf-N/O-C. a) Synthesis route of single-atomically dispersed Hf catalyst. b) STEM image and corresponding energy-dispersive spectroscopy (EDS) elemental maps of s-Hf-N/O-C. c) Aberration-corrected high-angle annular dark-field scanning transmission electron microscopy (AC–HAADF–STEM) image identifying bright Hf atoms atomically dispersed in or on graphene layers. d) Hf L_3-edge X-ray absorption near-edge spectra (XANES) spectra. e) Fourier-transformed extended X-ray absorption fine structure (EXAFS) in R-space. $\chi(R)$ is the magnitude of the Fourier transform of the extended X-ray absorption fine structure. X, μ, and E are the absorption length, the absorption coefficient, and the energy of the X-rays, respectively. f–h) Wavelet transform (WT) EXAFS plots of the Hf foil, s-Hf-N/O-C, and HfO_2, respectively.

Additionally, N/O-doped graphene (N/O-C), graphene-supported atomically dispersed HfN_4 motifs (s-Hf-N-C), and N-doped graphene-supported HfO_2 motifs (HfO_2-N-C) were prepared for comparison. Two other subgroup-IVB single-atom catalysts (s-Zr-N/O-C and s-Ti-N/O-C) were also synthesized with the same method. Appealingly, a 20-fold increase in the scale of the synthetic experiment was achieved (Figure S8, Supporting Information).

Representative scanning electron microscopy (SEM) images showed that typical 3D honeycomb graphene structures remained after removing the oxide particles (Figure S9a,b, Supporting Information). As shown with the Brunauer–Emmett–Teller (BET) method (Figure S9c,d, Supporting Information), the N_2 isotherms for s-Hf-N/O-C at 77 K were type-I isotherms corresponding to microspores and then converted to type-IV isotherms with hysteresis, which indicated mesopores from oxide aggregation.[25] Similar BET data were observed for N/O-C, indicating that Hf doping hardly affected the 3D honeycomb structure of the graphene substrate. This was confirmed with high-resolution transmission electron microscopy (HRTEM) (Figure S10, Supporting Information); this showed that no clusters or nanoparticles were present in s-Hf-N/O-C substrate, which resembled the pure carbon layers in N/O-C. Both the STEM image and the corresponding energy-dispersive spectroscopy (EDS) elemental maps (Figure 2b,c) for s-Hf-N/O-C showed that there were numerous atomically dispersed metal atoms (bright dots) on the s-Hf-N/O-C substrate, unlike the pure carbon layers in N-C. The aberration-corrected high-angle annular dark-field scanning transmission electron microscopy (AC–HAADF–STEM) image (Figure 2c) showed that the atomically dispersed Hf sites were uniformly anchored on the N, O codoped graphene support. The Hf content in s-Hf-N/O-C is 5.08 wt%, as determined with inductively coupled plasma-mass spectrometry (ICP–MS) (Table S2, Supporting Information). A similar morphology was also observed for the s-Hf-N-C sample (Figure S11, Supporting Information).

X-ray photoelectron spectroscopy (XPS) and X-ray absorption spectra (XAS) were used to clarify the structure of the s-Hf-N/O-C catalyst. The XPS spectrum (Figure S12, and Tables S3–S5 Supporting Information) confirmed that s-Hf-N/O-C contained Hf, N, O, and C atoms. Furthermore, the Hf 4f XPS peaks positions for s-Hf-N/O-C appeared between those for the HfO_2-N-C and s-Hf-N-C, implying that the Hf oxidation state was lower than +4 due to the presence of a unique N-Hf-O coordination environment. This was also confirmed with FTIR and Raman spectroscopy, wherein the signals for HfO_2 particles were hardly observed (Figure S13a,b, Supporting Information).

Additionally, according to the Hf L_3-edge X-ray absorption near-edge spectra (XANES) (Figure 2d), the oxidation states for the Hf single atoms, determined from the white-line intensity of the Hf L_3-edge, increased in the order Hf foil (0) < s-Hf-N-C < s-Hf-N/O-C < HfO_2 (+4), revealing that the axial O atoms regulated the oxidation states of the Hf sites.[26] Additionally, extended X-ray absorption fine structure (EXAFS) data were collected to determine the coordination configurations, includ-ing the coordination numbers and bond lengths. The Fourier transformed (FT) L_3-weighted EXAFS spectrum of s-Hf-N-C exhibited a prominent peak at 1.60 Å, which was attributed to Hf-N bonds (Figure 2e). Moreover, the first peak for s-Hf-N/O-C broadened and was shifted positively relative to that for s-Hf-N-C, indicating a different coordination structure resulting from the axial oxygen. In addition, Hf-Hf bonds were not detected for s-Hf-N/O-C and s-Hf-N-C (Figure 2e), demonstrating that the Hf species were isolated in these systems. It is worth noting that the peak is unsymmetrical and shifted slightly, implying that a higher Hf coordination number generated out-of-graphene plane distortions.[27] The results obtained for s-Hf-N/O-C with quantitative EXAFS fitting revealed that Hf was coordinated by approximately four coplanar N atoms (coordination number: 4.2) with bond lengths of 2.05 Å and approximately one axial O atom (coordination number: 1) with a bond length of 1.93 Å (Figure S14a and Table S6, Supporting Information). The fitted k-space curve (Figure S14b, Supporting Information) was consistent with the experimental data. Additionally, we performed a wavelet transform (WT) for the EXAFS oscillations of s-Hf-N/O-C to visualize the dispersed metal atom sites with high resolution for the radial distance and k-space (Figure 2f–h). s-Hf-N/O-C dis-played the maximum intensity at approximately 3.9 Å^{-1}, which was quite different from Hf-Hf bonds (≈ 5.9 Å^{-1}) somewhat different from Hf-O bonds (≈ 4.5 Å^{-1}). Additionally, ultravi-olet photoelectron spectroscopy (UPS) showed a significantly lower work function for s-Hf-N/O-C, compared to those of both s-Hf-N-C and HfO_2-N-C (Figure S13c, Supporting Information), suggesting that the Hf coordination structure in s-Hf-N/O-C was completely different from those of s-Hf-N-C or HfO_2-N-C.[28]

2.3. Catalytic Performance

The ORR activities of the s-M-N/O-C (M = Ti, Zr, Hf) catalysts were investigated with a rotating ring-disk electrode (RRDE) in a standard three-electrode system containing a O_2-saturated 0.1 м aqueous KOH. All electrode potentials were referenced to the reversible hydrogen electrode (versus RHE). The cyclic voltammograms (Figure S15a,b, Supporting Information) showed obvious cathodic peaks for the s-Hf-N/O-C and s-Hf-N-C catalysts under O_2. As evidenced by linear sweep voltammetry (**Figures 3**a and S15c,d, Supporting Information), the half-wave potentials ($E_{1/2}$ = 0.920 V) and onset potentials (E_{onset} = 1.050 V) of s-Hf-N/O-C indicated excellent ORR activity surpassing those of s-Hf-N-C ($E_{1/2}$ = 0.821 V, E_{onset} = 0.915 V), N/O-C ($E_{1/2}$ = 0.811 V, E_{onset} = 0.896 V), commercial Pt/C ($E_{1/2}$ = 0.850 V, E_{onset} = 0.961 V), and previously reported nonprecious metal catalysts (Figure 3b and Table S7, Supporting Information). Consistent with the DFT calculations, s-Ti-N/O-C and s-Zr-N/O-C also exhibited significantly higher activities than a commercial Pt/C catalyst. (Figure S17a,d, Supporting Information). According to RRDE and Koutecky–Levich (K–L) equation results (Figure 3c and Figure S16, Supporting Information), the electron-transfer rate for s-Hf-N/O-C was close to 4, and the H_2O_2 yield was below 3.5%at 0.8 V, which confirmed an efficient four-electron pathway for s-Hf-N/O-C catalysis of the ORR. This unique ORR activity was also indicted by the small Tafel slopes (43.18 mV dec^{-1}) and the large double-layer capacitance (C_{dl}) of 55.40 mF cm^{-2} (Figure 3d and Figure S17e,f, Supporting Information), indicating a small energy barrier and a high electrochemical surface area.[29]

In addition, stability is another important parameter used to assess the ORR activities of electrocatalysts. Similar to Ti-N/O-C and s-Zr-N/O-C, accelerated durability tests (ADT) showed that the performance decline of s-Hf-N/O-C was negligible after 5000 cycles, as confirmed by the small potential drop (14 mV) after 15000 cycles, (Figures 3e and S18a,b, Supporting Information) and the high current density retention rate (95.4%) after a chronoamperometry (CA) study of 18000 s (Figure S18c, Supporting Information). Furthermore, as shown in the ICP-MS (Table S8, Supporting Information) results, there was approximately zero residual Hf in the solution after 15000 CV cycles with s-Hf-N/O-C, which confirmed its excellent stability. Furthermore, the structure remained intact except for the few Hf atoms were oxidized (Figure S19 and Table S9, Supporting Information), and this also confirmed the durability of the s-Hf-N/O-C catalyst. Fi-nally, the methanol cross-over effect showed excellent methanol tolerance for s-Hf-N/O-C, which showed an extremely similar CV curve and negligible decay in the current density after methanol was injected (Figure S20a,b, Supporting Information). Poisoning experiments were performed with potassium thiocyanate (KSCN) addition, since KSCN was known to complex transition metal ions strongly, poison the electrocatalytic centers, and decrease activities of single-atom catalysts. The substantially reduced $E_{1/2}$ and limited current density for s-Hf-N/O-C in a 0.1 м KOH solution with added KSCN proved that the active sites in the s-Hf-N/O-C ORR catalyst were HfN_4O sites (Figure S20c,d, Supporting Information).[30] The electrocatalytic information, including the $E_{1/2}$, Tafel slope, j_k, C_{dl}, and stabilities among Pt/C, s-Hf-N/O-C, s-Zr-N/O-C, and s-Ti-N/O-C are summarized in Figure 3f, which shows that s-Hf-N/O-C has higher ORR catalytic activity, stability, and lower toxicity than the other catalysts.
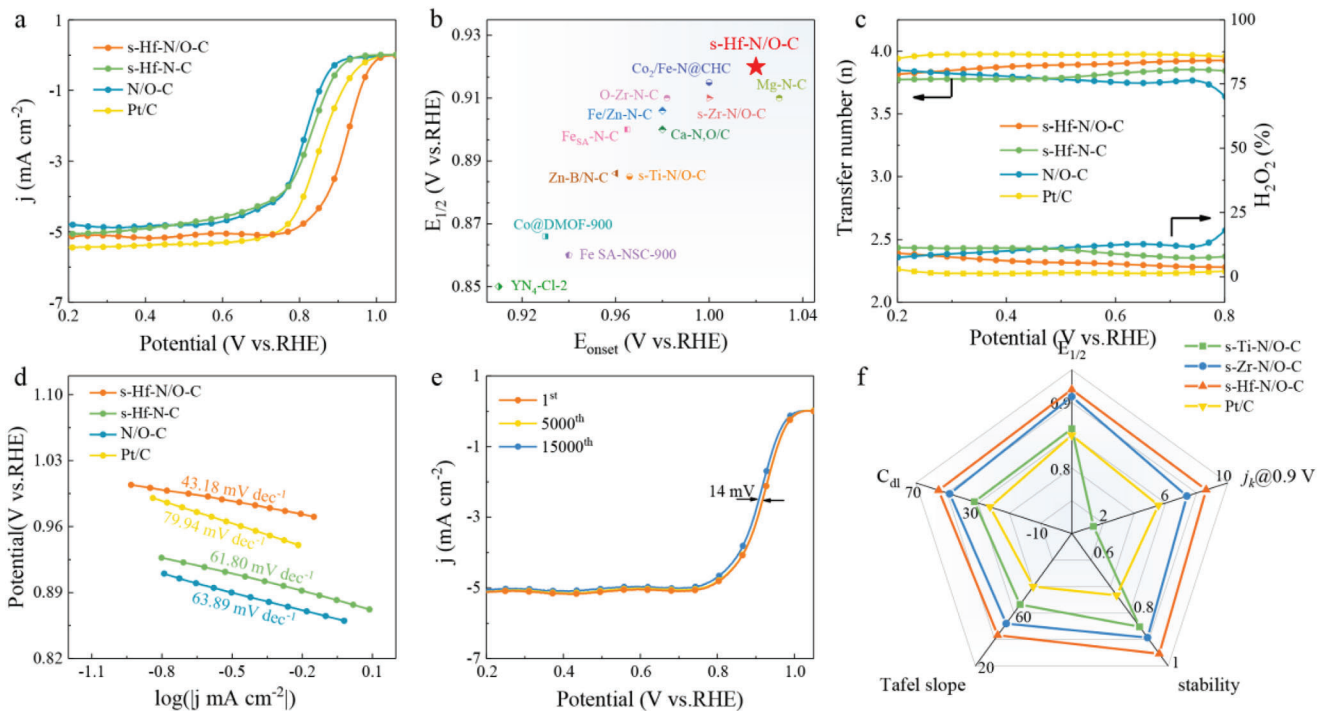
Figure 3. Oxygen reduction reaction (ORR) performance of the s-Hf-N/O-C catalyst. a) Steady-state RDE polarization curves in an O_2-saturated 0.1 M KOH solution at 1600 rpm and 10 mV s^{-1}. b) Comparison of s-Hf-N/O-C with the other reported single-atom catalysts for the ORR. c) The H_2O_2 yield and the electron transfer rate. d) Tafel plots. e) Initial activity and stability results of s-Hf-N/O-C from the accelerated durability tests (ADT) by cycling the potentials (0.6–1.0 V, 5000 and 15 000 cycles) in an O_2-saturated 0.1 M KOH solution. The black arrows indicate the activity loss concerning the negative shifts of half-wave potentials. f) Comparison of $E_{1/2}$, j_k @ 0.9 V, Tafel slope, C_{dl}, and stability for the catalysts.

In situ surface-enhanced Raman scattering (SERS) in a O2- saturated 0.1 M KOH was used to determine the atomic and electronic structure of s-Hf-N/O-C under ORR conditions(**Figure 4**a). As illustrated in Figure 4b, except for the carbon peak at 1640 cm^{-1}, a peak appeared at approximately 1070 cm^{-1} for the pure Hf-N-C sample as the potential was decreased, corresponding to the *OH intermediate.[31] The *OH peak intensity increased slightly, indicating that the conversion of *O to *OH was on the HfN$_4$ active centers (Figure 4c). The slight difference in peak intensity reflected the low catalytic activity of the Hf-N-C catalyst, which was consistent with the DFT predictions. In comparison, in addition to the 1350 and 1600 cm^{-1} that belonged to the carbon peaks, two main peaks were observed for s-Hf-N/O-C (Figure 4d), which were assigned to the O-O vibrations of *O^{2-} (1165 cm^{-1}) and *OOH (1525 cm^{-1}).[32] The *OOH peaks were detected for both samples (Figure 4e,f). The peak position for the *OOH in s-Hf-N/O-C was significantly shifted to the left compared with that for the N/O-C sample, signifying that the presence of *OOH was associated with the Hf-N/O active sites and the N/O-C catalyst itself (Figure 4f). To assess the contributions of the Hf-N/O active sites in *OOH formation, we quantitatively com-pared the potential-dependent Raman peak intensities for ORR intermediates on the Hf-N/O moiety after eliminating the effect of N/O-C (Figure 4e). The higher fraction of *OOH showed that the formation of *OOH was the RDS of the ORR catalyzed with Hf-N/O under alkaline conditions,[33] which was consistent with the outcomes described above.

2.4. Battery Performance

To examine the viability of using the s-Hf-N/O-C catalyst in real devices, we tested a Zn-air battery (ZAB) with a cathode con-taining s-Hf-N/O-C. The ZAB with the s-Hf-N/O-C electrode (**Figure 5**a) showed a high open-circuit voltage of 1.49 V, which exceeded those of ZABs equipped with the Pt/C benchmark electrode (1.44 V). Additionally, the cycling performance was investigated with galvanostatic charge–discharge cycles lasting 20 min per cycle (Figure 5b), and negligible voltage losses in the charge and discharge processes were observed after 1600 h for the s-Hf-N/O-C-containing ZAB. The discharge polarization plots (Figure 5c) illustrate that the s-Hf-N/O-C ZAB provides a higher discharge current with a peak discharge power density of 256.9 mW cm^{-2}, which is superior to the commercial Pt/C cath-ode (173.71 mW cm^{-2}). Then, stability tests indicated that the s-Hf-N/O-C-containing ZAB showed a staircase-like voltage re-sponse over 180 h (Figure 5d) when the discharge current density was varied from 5 to 20 mA cm^{-2} after every 100 cycles. Moreover, the s-Hf-N/O-C-based ZAB exhibited stable operation (at 20 °C, 50 °C, 20 °C, −10 °C, and 20 °C, sequentially) and maintained a lower overpotential than the Pt/C-based ZAB, illustrating its promise for use on a large scale (Figure 5e).
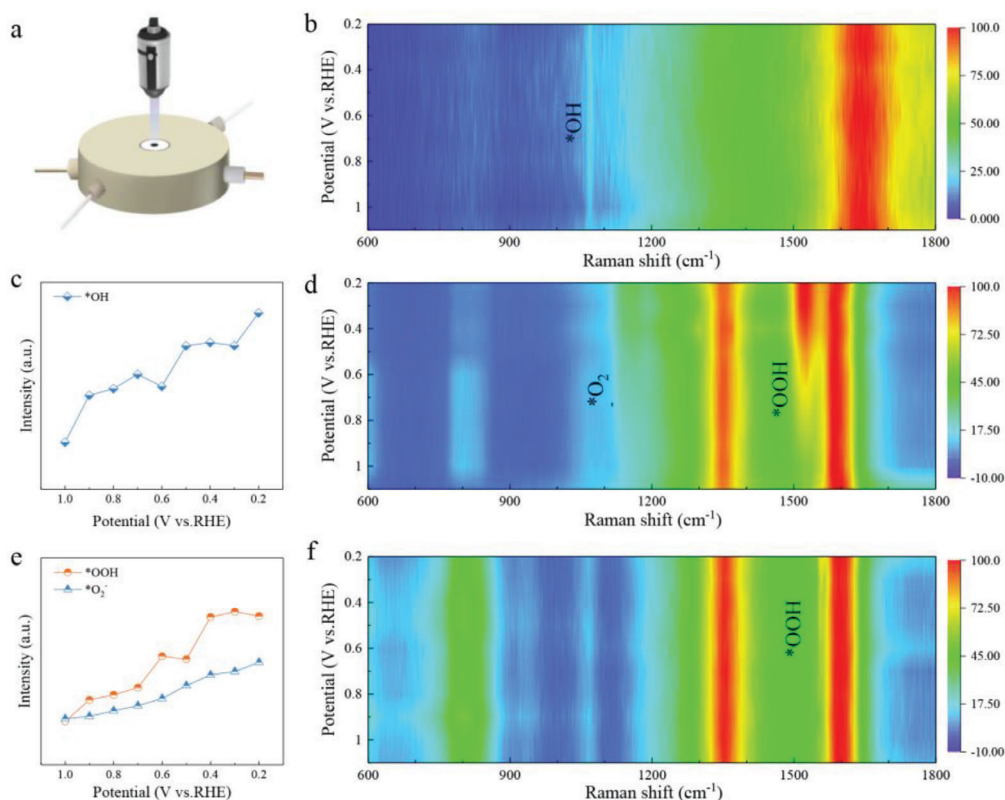
Figure 4. In situ catalytic mechanism. a) Schematic diagram of in situ Raman testing. b) In situ electrochemical Raman spectra of Hf-N-C. c) Intensity changes of *OH peak of Hf-N-C after magnification by 10 times. d) In situ electrochemical Raman spectra of s-Hf-N/O-C. e) Intensity changes of *OOH and *O$_2^-$ peaks in s-Hf-N/O-C were amplified twice after eliminating the effect of N/O-C. f) In situ electrochemical Raman spectra of N/O-C.

To determine the role of s-Hf-N/O-C in the air cathode, in situ XRD spectra were obtained to identify the structural and chemical transformations occurring inside the battery during operation (Figure 5f). The bonding mode for oxygen chemisorbed on the carbon surface can be either end-on (Pauling model) or side-on (Yeager model)[34] due to charge delocalization. Oxy-gen molecules and oxygen-containing intermediates gradually adjusted the carbon through continuous chemisorption during the discharge process, resulting in a gradual weakening of the peak intensity. The changes in the carbon peak for the N/O-C-based ZAB were indistinct (Figure 5g), revealing that this sample had low catalytic activity and was not the major active site. Notably, akin to the N/O-C electrode, the original state of the s-Hf-N/O-C cathode displayed one major diffraction peak at ≈26°relative to carbon. However, the 26° peak for the ZAB contain-ing s-Hf-N/O-C gradually weakened during the discharge process (Figure 5h), which enabled continuous de/adsorption of oxygen molecules and oxygen-containing intermediates during the ORR process.[35]

3. Conclusion

This contribution reported a common strategy involving axial-group modification of d-orbitals to create catalytic cores containing subgroup-IVB elements, which is also possible for other transition metals. The properties predicted with the DFT calculations were confirmed experimentally. The distinct dual-ligand confining structure of HfN$_4$O was clarified with HRTEM, XPS, XANES, and EXAFS studies. In particular, the pentacoordinate s-Hf-N/O-C catalyst (with four coplanar Ns and one out-of-plane O ligand) containing 5.08 wt % Hf showed good electrocatalytic activity and good cycling stability, which exceeded those of the Pt/C catalyst based on the four-electron reduction path-way and ZAB power density. In situ SERS confirmed that Hf-N/O-C with a pentacoordinate structure reduced the adsorption strengths of *OH intermediates and enhanced the ORR activi-ties. The discovery of unique subgroup-IVB SACs with high activities and stabilities for the ORR provides a promising substitute for the expensive Pt-based catalysts in ZAB cathodes.
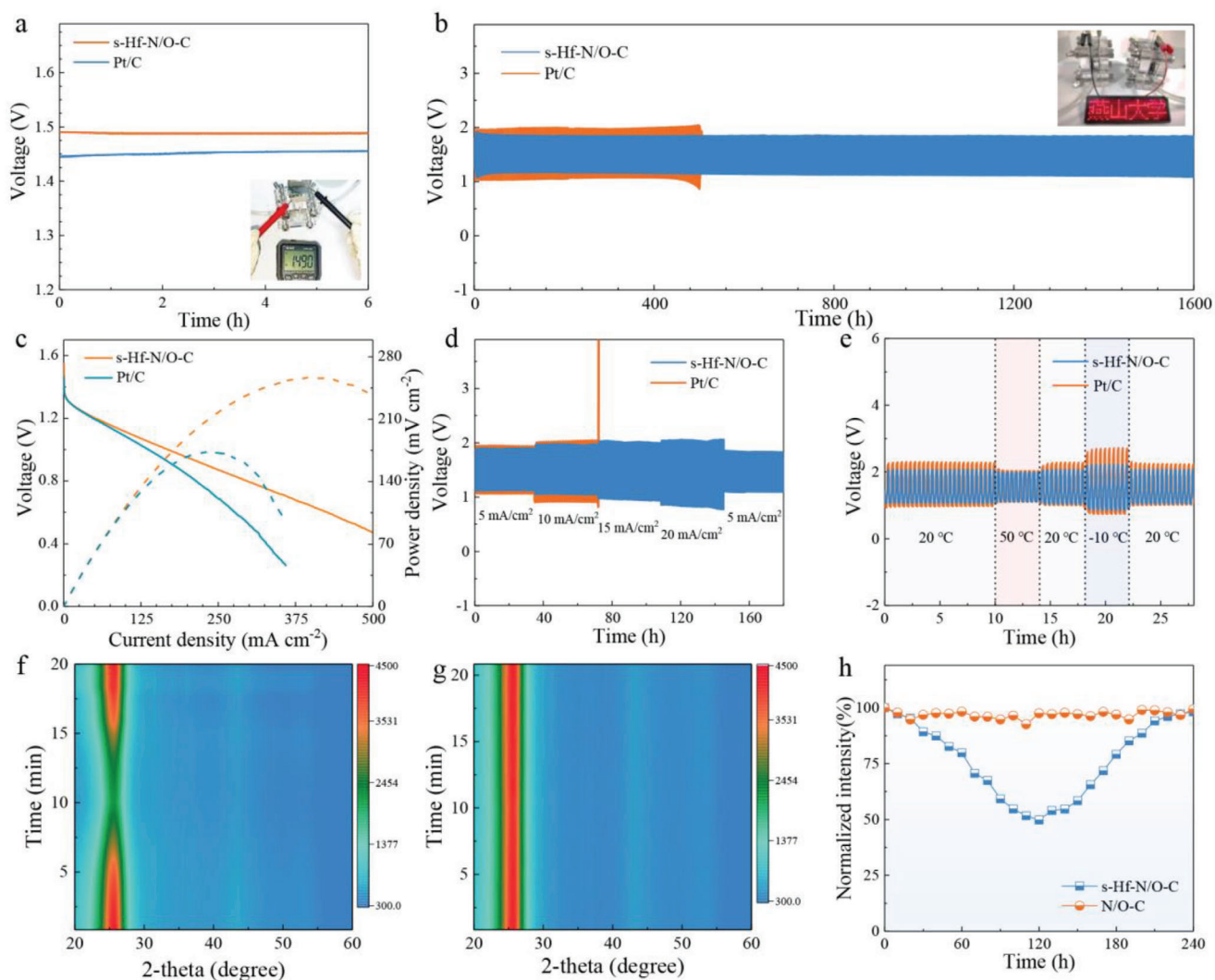
Figure 5. Aqueous Zn-air battery (ZAB) performance with s-Hf-N/O-C air cathode in comparison with noble metal of 40% Pt/C. a) Open circuit voltage curves. The inset shows the photograph of open circuit voltage of the ZAB with s-Hf-N/O-C air cathode. b) Long-term cyclic stability tests at a current density of 10 mA cm^{-2}. c) Discharge polarization curves and corresponding areal power density curves. d) The galvanostatic charge–discharge curves at room temperature with various current densities. e) The galvanostatic charge–discharge curves of 10 mA cm^{-2} at different temperatures. f,g) In situ X-ray diffraction (XRD) intensity map of ZABs with s-Hf-N/O-C and N/O-C electrodes during charge–discharge of 10 mA cm^{-2}. h) Intensity changes of the C peak at 26 °C of different air cathodes during ZAB operation.

Supporting Information

Supporting Information is available from the author.

Acknowledgements

Conflict of Interest

The authors declare no conflict of interest.

Data Availability Statement

Research data are not shared.

References

[1] Z. Liu, Z. Deng, G. He, H. Wang, X. Zhang, J. Lin, Y. Qi, X. Liang, *Nat. Rev. Earth Environ.* **2022**, *3*, 141.

[2] a) C. Chen, Y. Kang, Z. Huo, Z. Zhu, W. Huang, H. L. Xin, J. D. Snyder, D. Li, J. A. Herron, M. Mavrikakis, *Science* **2014**, *343*, 1339; b) M. K. Debe, *Nature* **2012**, *486*, 43; c) Y.-J. Wang, N. Zhao, B. Fang, H. Li, X. T. Bi, H. Wang, *Chem. Rev.* **2015**, *115*, 3433.

[3] F. Lu, Y. Zhang, S. Liu, D. Lu, D. Su, M. Liu, Y. Zhang, P. Liu, J. X. Wang, R. R. Adzic, *J. Am. Chem. Soc.* **2017**, *139*, 7310.

[4] a) X. F. Lu, B. Y. Xia, S. Q. Zang, X. W. Lou, *Angew. Chem., Int. Ed.* **2020**, *132*, 4662; b) J. Liu, M. Jiao, B. Mei, Y. Tong, Y. Li, M. Ruan, P. Song, G. Sun, L. Jiang, Y. Wang, *Angew. Chem., Int. Ed.* **2019**, *131*, 1175; c) X. Wang, Z. Li, Y. Qu, T. Yuan, W. Wang, Y. Wu, Y. Li, *Chem* **2019**, *5*, 1486.

[5] a) S. Liu, C. Li, M. J. Zachman, Y. Zeng, H. Yu, B. Li, M. Wang, J. Braaten, J. Liu, H. M. Meyer III, *Nat. Energy* **2022**, *7*, 652; b) J. Liu, X. Wan, S. Liu, X. Liu, L. Zheng, R. Yu, J. Shui, *Adv. Mater.* **2021**, *33*, 2103600; c) J. Chen, H. Li, C. Fan, Q. Meng, Y. Tang, X. Qiu, G. Fu, T. Ma, *Adv. Mater.* **2020**, *32*, 2003134; d) J. Li, M. Chen, D. A. Cullen, S. Hwang, M. Wang, B. Li, K. Liu, S. Karakalos, M. Lucero, H. Zhang, *Nat. Catal.* **2018**, *1*, 935.

[6] X. X. Wang, V. Prabhakaran, Y. He, Y. Shao, G. Wu, *Adv. Mater.* **2019**, *31*, 1805126.

[7] X. Xie, C. He, B. Li, Y. He, D. A. Cullen, E. C. Wegener, A. J. Kropf, U. Martinez, Y. Cheng, M. H. Engelhard, *Nat. Catal.* **2020**, *3*, 1044.

[8] H. Tian, A. Song, P. Zhang, K. Sun, J. Wang, B. Sun, Q. Fan, G. Shao, Chen, H. Liu, *Adv. Mater.* **2023**, *35*, 2210714.

[9] a) A. Ruban, B. Hammer, P. Stoltze, H. L. Skriver, J. K. Nørskov, *J. Mol. Catal. A: Chem.* **1997**, *115*, 421; b) J. K. Nørskov, F. Abild-Pedersen, F. Studt, T. Bligaard, *Proc. Natl. Acad. Sci. U. S. A.* **2011**, *108*, 937.

[10] W. Zhang, Y. Chao, W. Zhang, J. Zhou, F. Lv, K. Wang, F. Lin, H. Luo, Li, M. Tong, *Adv. Mater.* **2021**, *33*, 2102576.

[11] a) H. Shang, X. Zhou, J. Dong, A. Li, X. Zhao, Q. Liu, Y. Lin, J. Pei, Z. Li, Z. Jiang, *Nat. Commun.* **2020**, *11*, 3049; b) K. M. Zhao, S. Liu, Y. Y. Li, X. Wei, G. Ye, W. Zhu, Y. Su, J. Wang, H. Liu, Z. He, *Adv. Energy Mater.* **2022**, *12*, 2103588.

[12] B. Ji, J. Gou, Y. Zheng, X. Pu, Y. Wang, P. Kidkhunthod, Y. Tang, *Adv. Mater.* **2023**, *35*, 2300381.

[13] X. Wang, Y. An, L. Liu, L. Fang, Y. Liu, J. Zhang, H. Qi, T. Heine, T. Li, Kuc, *Angew. Chem., Int. Ed.* **2022**, *134*, 202209746.

[14] Y. Yuan, J. Wang, S. Adimi, H. Shen, T. Thomas, R. Ma, J. P. Attfield, Yang, *Nat. Mater.* **2020**, *19*, 282.

[15] a) X. Zhao, J. Wang, J. Wang, M. Yang, C. Yan, G. Zou, S. T. John, Fernandez, Q. Peng, *Cell Rep. Phys. Sci.* **2022**, *3*, 3. b) L. Yin, S. Zhang, M. Sun, S. Wang, B. Huang, Y. Du, *Adv. Mater.* **2023**, *35*, 2302485.

[16] G. Wang, X. Yang, R. Wang, J. Jia, *Phys. Chem. Chem. Phys.* **2023**, *25*, 27342.

[17] a) G. Zhou, P. Wang, H. Li, B. Hu, Y. Sun, R. Huang, L. Liu, *Nat. Commun.* **2021**, *12*, 4827; b) Y. L. Zhang, B. Liu, Y. K. Dai, Y. F. Xia, P. Guo, Y. Y. Liu, F. Kong, Q. Zhang, L. Zhao, Z. B. Wang, *Adv. Funct. Mater.* **2022**, *32*, 2209499.

[18] X. Li, T. Chen, B. Yang, Z. Xiang, *Angew. Chem., Int. Ed.* **2023**, *135*, 202215441.

[19] P. Cao, X. Quan, X. Nie, K. Zhao, Y. Liu, S. Chen, H. Yu, J. G. Chen, *Nat. Commun.* **2023**, *14*, 172.

[20] K. Liu, J. Fu, Y. Lin, T. Luo, G. Ni, H. Li, Z. Lin, M. Liu, *Nat. Commun.* **2022**, *13*, 2075.

[21] a) L. Peng, J. Yang, Y. Yang, F. Qian, Q. Wang, D. Sun-Waterhouse, L. Shang, T. Zhang, G. I. Waterhouse, *Adv. Mater.* **2022**, *34*, 2202544; b) B. Ji, J. Gou, Y. Zheng, X. Zhou, P. Kidkhunthod, Y. Wang, Q. Tang, Y. Tang, *Adv. Mater.* **2022**, *34*, 2202714; c) M. Wang, W. Yang, X. Li, Y. Xu, L. Zheng, C. Su, B. Liu, *ACS Energy Lett.* **2021**, *6*, 379; d) Q. Li, W. Chen, H. Xiao, Y. Gong, Z. Li, L. Zheng, X. Zheng, W. Yan, W. C. Cheong, R. Shen, *Adv. Mater.* **2018**, *30*, 1800588.

[22] R. Bashyam, P. Zelenay, *Nature* **2006**, *443*, 63.

[23] Y. Yang, S. Zhang, S. Wang, K. Zhang, H. Wang, J. Huang, S. Deng, B. Wang, Y. Wang, G. Yu, *Environ. Sci. Technol.* **2015**, *49*, 4473.

[24] a) Z. Sun, S. Fang, Y. H. Hu, *Chem. Rev.* **2020**, *120*, 10336; b) C. Li, X. Zhang, K. Wang, X. Sun, G. Liu, J. Li, H. Tian, J. Li, Y. Ma, *Adv. Mater.* **2017**, *29*, 1604690.

[25] L. Song, J. Zhang, L. Sun, F. Xu, F. Li, H. Zhang, X. Si, C. Jiao, Z. Li, S. Liu, *Energy Environ. Sci.* **2012**, *5*, 7508.

[26] D. Cao, H. Xu, H. Li, C. Feng, J. Zeng, D. Cheng, *Nat. Commun.* **2022**, *13*, 5843.

[27] R. Jiang, L. Li, T. Sheng, G. Hu, Y. Chen, L. Wang, *J. Am. Chem. Soc.* **2018**, *140*, 11594.

[28] J. Chang, G. Wang, M. Wang, Q. Wang, B. Li, H. Zhou, Y. Zhu, W. Zhang, M. Omer, N. Orlovskaya, *Nat. Energy* **2021**, *6*, 1144.

[29] S. Liu, Z. Li, C. Wang, W. Tao, M. Huang, M. Zuo, Y. Yang, K. Yang, L. Zhang, S. Chen, *Nat. Commun.* **2020**, *11*, 938.

[30] C. Tang, A. E. Surkus, F. Chen, M. M. Pohl, G. Agostini, M. Schneider, H. Junge, M. Beller, *Angew. Chem., Int. Ed.* **2017**, *129*, 16843.

[31] M. Chen, Y. He, J. S. Spendelow, G. Wu, *ACS Energy Lett.* **2019**, *4*, 1619.

[32] G. Chen, T. Wang, P. Liu, Z. Liao, H. Zhong, G. Wang, P. Zhang, M. Yu, E. Zschech, M. Chen, *Energy Environ. Sci.* **2020**, *13*, 2849.

[33] Y. Pan, X. Ma, M. Wang, X. Yang, S. Liu, H. C. Chen, Z. Zhuang, Y. Zhang, W. C. Cheong, C. Zhang, *Adv. Mater.* **2022**, *34*, 2203621.

[34] C. Tang, Q. Zhang, *Adv. Mater.* **2017**, *29*, 1604103.

[35] M. Wang, W. Wang, T. Qian, S. Liu, Y. Li, Z. Hou, J. B. Goodenough, P. M. Ajayan, C. Yan, *Adv. Mater.* **2019**, *31*, 1803339.

Supplementary Information

Regulating *d*-Orbital Hybridization of Subgroup-IVB Single Atoms for Efficient Oxygen Reduction Reaction

Xue Zhao[†], Yong Sun[†], Jinming Wang, Anmin Nie, Guodong Zou,* Liqun Ren, Jing Wang, Yong Wang, Carlos Fernandez, Qiuming Peng*

X. Zhao, Y Sun, J. M. Wang, A.M. Nie, G.D. Zou, J. Wang, Q.M. Peng

State Key Laboratory of Metastable Materials Science and Technology, Yanshan University, Qinhuangdao, 066004, P.R. China

Corresponding Authors: zouguodong@ysu.edu.cn; pengqiuming@ysu.edu.cn

L.Q. Ren

Laboratory of Spinal Cord Injury and Rehabilitation, Chengde Medical University, Chengde, 067000, P.R. China

Y. Wang

College of Chinese Medicine, Beijing University of Chinese Medicine, Beijing, 100029, China

C. Fernandez

School of Pharmacy and life sciences, Robert Gordon University, Aberdeen, AB107GJ, United Kingdom

[†] These authors contributed equally to this work.

1. Methods

1.1 Computational method 1. All spin-polarized density-functional theory (DFT) computations were performed using the Vienna *ab-initio* simulation package (VASP) based on the projector augmented wave (PAW) method[1]. Electron-ion interaction was described using standard PAW potentials. A plane-wave basis set was employed to expand the smooth part of the wave functions with a cutoff kinetic energy of 400 eV. For the electron-electron exchange and correlation interactions, the functional parametrized by Perdew-Burke-Ernzerhof (PBE) and a form of the general gradient approximation (GGA) were used[2]. To probe the mechanism of surface reaction, the surface was set with a slab model. A sufficiently large vacuum region of 15 Å was used. During the geometry optimization, all atoms were allowed to relax. The Brillouin-zone integration was conducted using Monkhorst-Pack grids of special points with a separation of 0.06 Å^{-1}. The convergence criterion for the electronic self-consistent loop was set to 10^{-5} eV. The atomic structure was optimized until the residual force was below 0.03 eV Å^{-1}. Both density of states (DOS) and partial density of state (PDOS) were calculated under the HSE06 level for higher accuracy.

1.2 Computational method 2. The van der Waals (vdW) interaction was involved *via* the semi-empirical DFT-D2 field method[3]. The Gibbs free energy was calculated by the following equation:

$$\Delta G = \Delta E + \Delta ZPE - T\Delta S \qquad (1)$$

where ΔE was the adsorption energy difference from the initial state to the final state calculated by the DFT. ΔZPE and ΔS were the change in zero point energy (ZPE) and entropy due to the reaction. T was fixed at 289.15 K. The nature of the stationary point and ZPE corrections were characterized by calculating harmonic vibration frequency. Gibbs free energy change (ΔG_i, i = 1-4) for ORR can be calculated using

the following equations:

$$\Delta G_1 = 4.92 - \Delta G_{*OOH} \qquad (2)$$

$$\Delta G_2 = \Delta G_{*OOH} - \Delta G_{*O} \qquad (3)$$

$$\Delta G_3 = \Delta G_{*O} - \Delta G_{*OH} \qquad (4)$$

$$\Delta G_4 = \Delta G_{*OH} \qquad (5)$$

The theoretical overpotential η^{ORR} for a given electrocatalyst can be evaluated as the following equation:

$$\eta^{ORR} = 1.23 \text{ V} - min\{\Delta G_1, \Delta G_2, \Delta G_3, \Delta G_4\}/e \qquad (6)$$

1.3 Synthesis of catalysts. 0.96 g Mg powders (Aladdin, 99%) and 0.072 g HfCl$_4$ (Sigma, 98%) were added to stainless steel tank and milled for 10 h using a high-energy ball mill (Hi-Energy/Mill 8000D, Qingdao Lepike Electronics Co., LTD, China). After milling, the obtained mixed powders were gently scraped out and transferred to a graphite boat. The whole process was done in the glove box filled with argon (Ar) gas. Then, the graphite boat was placed in a tube furnace, heated to 900 °C for 5 h with a heating rate of 20 °C min^{-1} under a gas flow of CO$_2$/NH$_3$ (volume ratio of 1:1). Finally, s-Hf-N/O-C was obtained after removing the redundant oxide in a 10 wt.% HF solution for 8 h. The product obtained by oxidation with H$_2$O$_2$ after removing only MgO by pickling and H$_2$O$_2$ was HfO$_2$-N-C. The synthesis processes of s-Zr-N/O-C and s-Ti-N/O-C were similar to that of s-Hf-N/O-C, wherein ZrCl$_4$ and TiCl$_4$ were used instead of HfCl$_4$. For comparison, N/O-C was synthesized using Mg powders without any additives as the precursor. s-Hf-N-C was synthesized by the dissolution-and-carbonization method according to the reported research[4]. Specifically, glucose (C$_6$H$_{12}$O$_6$) was dissolved in ethanol, while HfCl$_4$ and hydroxylamine hydrochloride ((NH$_3$OH)Cl) were ultrasonically dissolved in

deionized water. Subsequently, the ethanol and water solutions were mixed. The mixture was then dried and heated to 600 °C under an Ar atmosphere, where it was maintained for 4 hours to achieve carbonization. Thus, the resultant product corresponds to the s-Hf-N-C, featuring HfN_4 coordination.

1.4 Material characteristics. XRD was performed by the SmartLab equipment (Rigaku, Japan) with Cu Kα radiation (λ = 1.5406 Å) in a 2θ range from 10° to 60° with a scanning rate of 4° min^{-1}. The morphology was observed by HRTEM-STEM at a voltage of 300 kV (JEOL2100, Japan). ICP-MS was measured by Agilent 7700/7800 (Agilent Technologies Co. Ltd., USA). XPS was operated on an ESCALAB 250 Xi (Thermo SCIENTIFIC, USA) using Al Kα radiation. FT-IR spectrometers were investigated by Nexus 870 (Thermo SCIENTIFIC, USA). Raman was obtained from inVia Qontor (Renishaw England). UPS measurement was carried out by ESCALAB 250Xi (Thermo SCIENTIFIC, USA). XAS was collected on the beamline BL07A1 in National Synchrotron Radiation Research Center (NSRRC). The radiation was monochro-matized by a Si (111) double-crystal monochromator. The acquired EXAFS data were processed according to the standard procedures using the ATHENA module implemented in the IFEFFIT software packages[5]. XANES and EXAFS data reduction and analysis were processed by Athena software. The $\chi_{(k)}$ data were Fourier transformed to real (R) space using a hanging windows (d_k = 1.0 Å^{-1}) to separate the EXAFS contribution from different coordination shells. The quantitative information can be obtained by the least-squares curve fitting in the R space with a Fourier transform k space range of 2.0-15 Å^{-1}, using the module ARTEMIS of programs of IFEFFIT. The backscattering amplitude $F_{(k)}$ and phase shift $\Phi_{(k)}$ were calculated using FEFF8.0 code.

1.5 Electrochemical properties. The ORR electrochemical measurements were

carried out on an electrochemical workstation (CHI 760E, China) equipped with a RRDE-3A (ALS Co., Ltd, Japan) using a standard three-electrode system. The glassy carbon (GC) with a diameter of 3 mm was used as the support for the working electrode. The graphite rod and Ag/AgCl electrode were utilized as the counter electrode and reference electrode, respectively. All the potentials were calibrated to the RHE potential calculated from the following equation:

$$E(vs.RHE) = E(vs.Ag/AgCl) + 0.198V + 0.059 \times pH \qquad (7)$$

All the potentials in this study were quoted vs. RHE. The catalyst ink was fabricated by mixing catalyst powders (5 mg) with a mix solution (200 μL isopropanol, 800 μL H_2O and 20 μL Nafion solution) under ultrasonic condition for 30 min. The ink was drop-casted on the disk electrode with a controlled loading of 0.6 mg cm^{-2} and dried at room temperature to yield a thin film electrode. Before the measurement, a stream of Ar or O_2 flow was delivered to the electrolyte for 30 min to obtain an Ar or O_2-saturated solution. The ORR curves were acquired under O_2-saturated condition by subtracting the data under Ar-saturated condition as a background. cyclic voltammetry (CV) measurement was carried out in the Ar or O_2 saturated 0.1 M KOH solutions at a scanning rate of 50 mV s^{-1} in a cycling potential between 0 V and 1.2 V. The catalytic activity of samples was evaluated by using linear sweep voltammetry at a scan rate of 10 mV s^{-1} with different rotation rates (400 to 2025 rpm).

For the ORR at a RRDE, the electron transferred number (n) and kinetic current density (j_k) were calculated according to the Koutecty-Levich (K-L) plots linear fit lines from the K-L equation:[6]

$$\frac{1}{j} = \frac{1}{j_L} + \frac{1}{j_K} = \frac{1}{B\omega^{1/2}} + \frac{1}{j_K} \qquad (8)$$

$$B = 0.62nFD_0^{2/3}v^{-1/6}C_0 \qquad (9)$$

where j was the current density measured from the ORR, j_L and j_k represented the diffusion-limiting, and the kinetic current density, respectively. ω was the angular velocity of the disk, F was the Faraday constant (F = 96485 C mol^{-1}), D_0 was the diffusion coefficient of O$_2$ (1.9×10^{-5} cm^2 s^{-1}), C_0 was the bulk concentration of O$_2$ (1.2×10^{-6} mol cm^{-3}) and V was the kinematic viscosity of the electrolyte (0.01 cm^2 s^{-1}). For the RRDE tests, the hydrogen peroxide yield [H$_2$O$_2$(%)] and the electron transfer number (n) can be calculated from the LSV at 1600 rpm via the following equations:

$$H_2O_2(\%) = 200 \times \frac{\dfrac{I_r}{N}}{I_d + \dfrac{I_r}{N}} \qquad (10)$$

$$n = 4 \times \frac{I_d}{I_d + \dfrac{I_r}{N}} \qquad (11)$$

where I_d was the disk current, I_r was the ring current and N was the current collection efficiency of the platinum ring with a value of 0.4.

1.6 *In-situ* surface-enhanced Raman scattering (SERS). *In-situ* SERS measurement was conducted on the Renishaw inVia Qontor confocal Raman microscope (50X objective) using a 532 nm laser light at a power of 10 mW, equipped with a modified electrochemical Raman cell. 5 μL of shell-isolated nanoparticles (SHINs) (Nanjing Kike Biotechnology Co., LTD) was deposited on a glassy carbon electrode and was dried at room temperature. To prevent the interference of surfactants and other impurities, electrochemical cleaning was performed at close to hydrogen evolution potential for 5 minutes. Then the electrode was washed with deionized water, and the alkaline electrolyte in electrochemical cell

was renewed. This process was repeated 3-5 times. The solution of Raman experiment was performed in a 0.1 M $NaClO_4$ solution (pH ≈ 9). Finally, the electrode was transferred to another clean Raman cell with a 0.1 M KOH solution (O_2 saturated) for SERS tests. The average values were obtained in terms of three measurements after holding at each potential for 10 min between 1.0 and 0.2 V.

1.7 ZAB performance. The temperature was controlled by a programmable box (GDJS-100, Beijing YaShiLin Testing Equipment Co., Ltd., China). 6 M KOH with 0.2 M $Zn(CH_3COOH)_2$ was the electrolyte, while the polished zinc plate was used as the anode. The air cathode was made by drop casting the catalyst ink which consists of the catalysts, ionomer (Nafion solution, 5 wt %), isopropanol and H_2O onto the hydrophilic carbon paper with a mass loading of 1.0 mg cm^{-2}. The polarization curves were obtained by using the CHI760E electrochemical workstation, and the galvanostatic charge-discharge tests were performed on a battery measurement system (Land CT2001A, China).

1.8 *In-situ* XRD. *In-situ XRD* measurement was performed on Rigaku SmartLab equipped with a home-made multifunctional electrochemical *in-situ* X-ray diffraction mold for batteries. The Zn-air battery (ZAB) using for *in-situ* XRD measurement was assembled with s-Hf-N/O-C, or N/O-C-coated carbon paper as air cathode, a Whatman glass microfiber filter (GF/D, thickness was 675 μm) as separator, a polished Zn plate (99.99%, thickness was 0.5 mm) as anode, and 6 M KOH with 0.2 M $Zn(CH_3COOH)_2$ as the electrolyte. The galvanostatic charge-discharge test was carried out by the CHI760E electrochemical workstation at a current density of 10 mA cm^{-2}. The XRD patterns recorded frequency at the same location was about 10 min within a 2θ range of 20° and 60° at a rate of 10° s^{-1}.

2. Results and Discussion
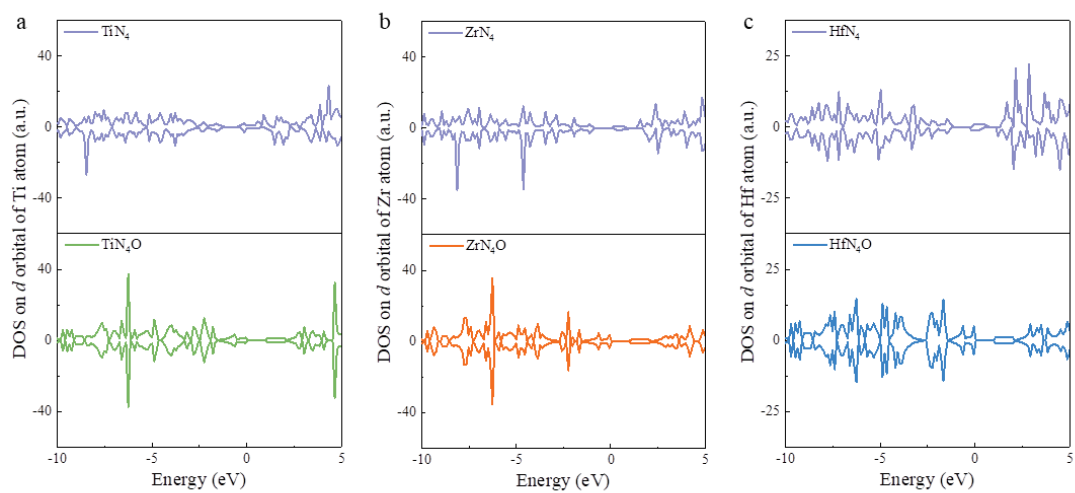
Figure S1. Density of states (DOS) on d-orbitals of subgroup-IVB moieties. (a-c) DOS of TiN_4 and TiN_4O, ZrN_4 and ZrN_4O, HfN_4 and HfN_4O, respectively.
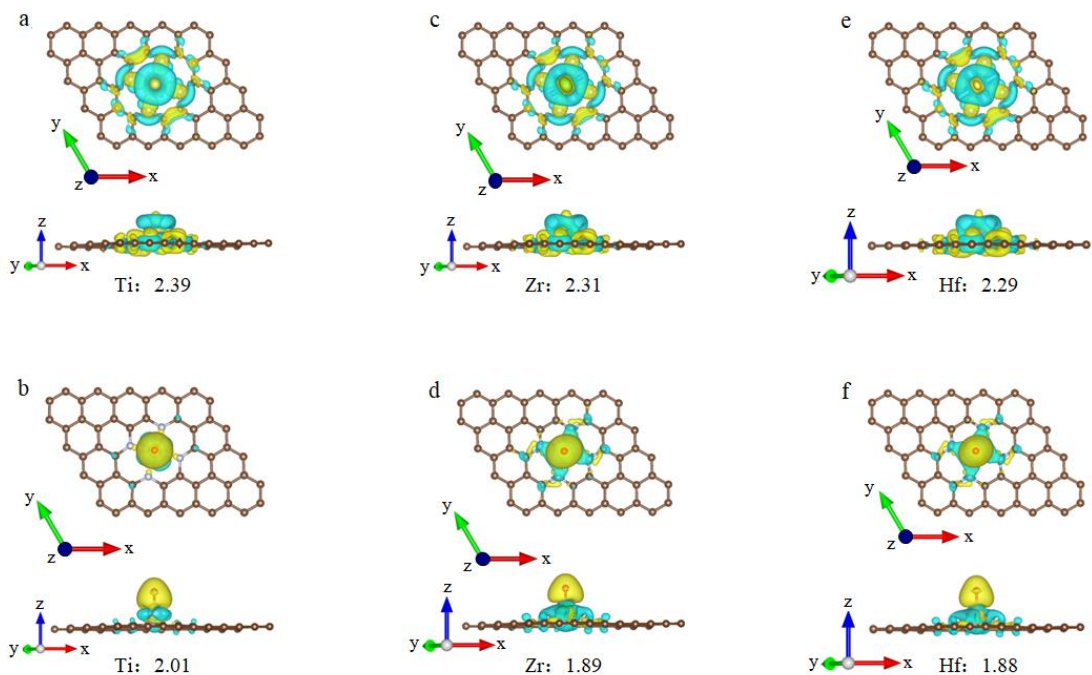
Figure S2. The charge distribution of subgroup-IVB moieties. (a-f) The differential charge density maps of TiN_4, TiN_4O, ZrN_4, ZrN_4O, HfN_4, and HfN_4O, respectively. The value represents the Bader charge.
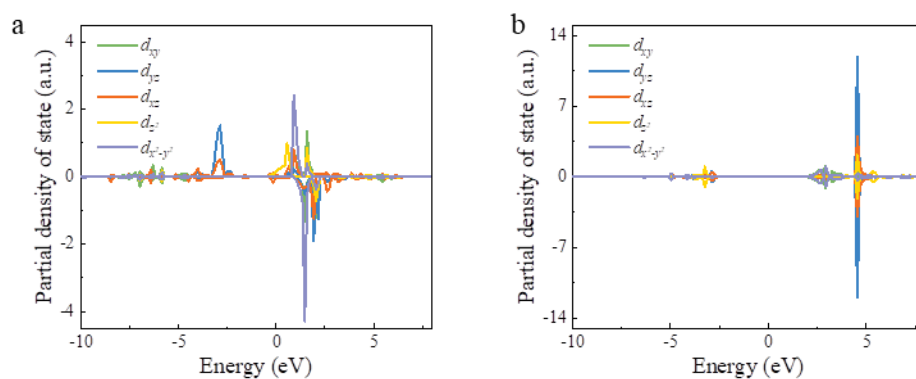
Figure S3. Charge transfer and orbital interactions of ORR on TiN_4 and TiN_4O. (a) PDOS on d-orbital of Ti for TiN_4. (b) PDOS on d-orbital of Ti for TiN_4O.
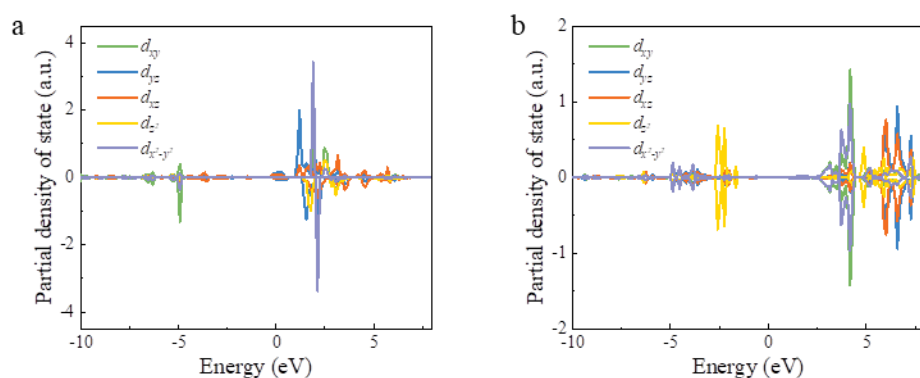
Figure S4. Charge transfer and orbital interactions of ORR on ZrN$_4$ and ZrN$_4$O. (a) PDOS on d-orbital of Zr for ZrN$_4$. (b) PDOS on d-orbital of Zr for ZrN$_4$O.
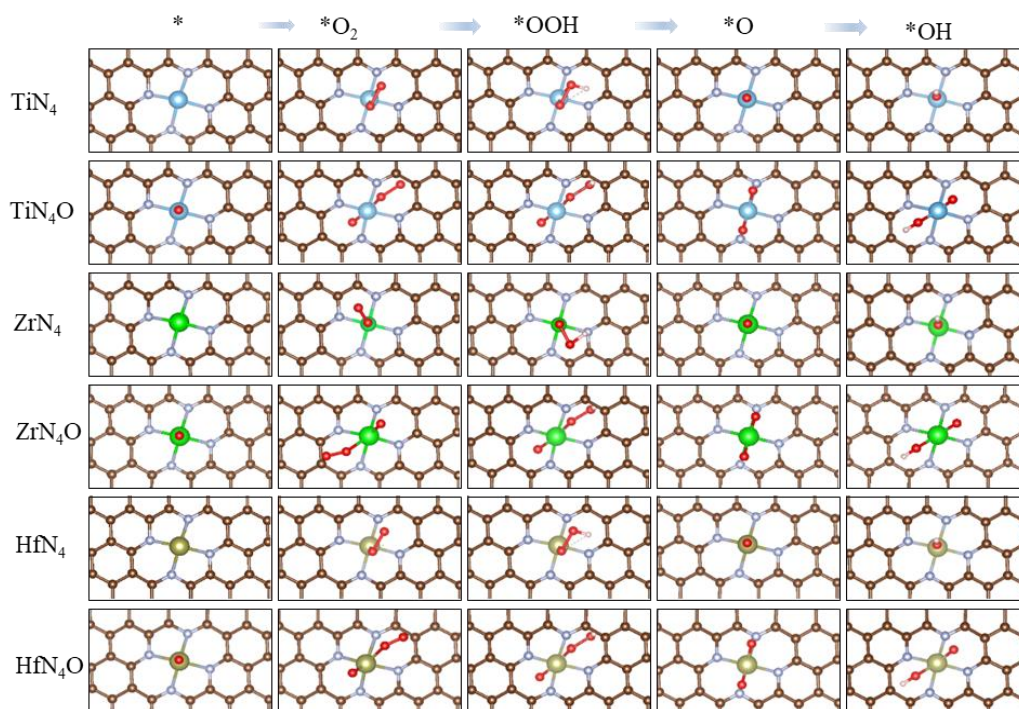
Figure S5. DFT calculation models. Proposed configurations for the reaction centers and the key reaction intermediates of subgroup-IVB moieties.
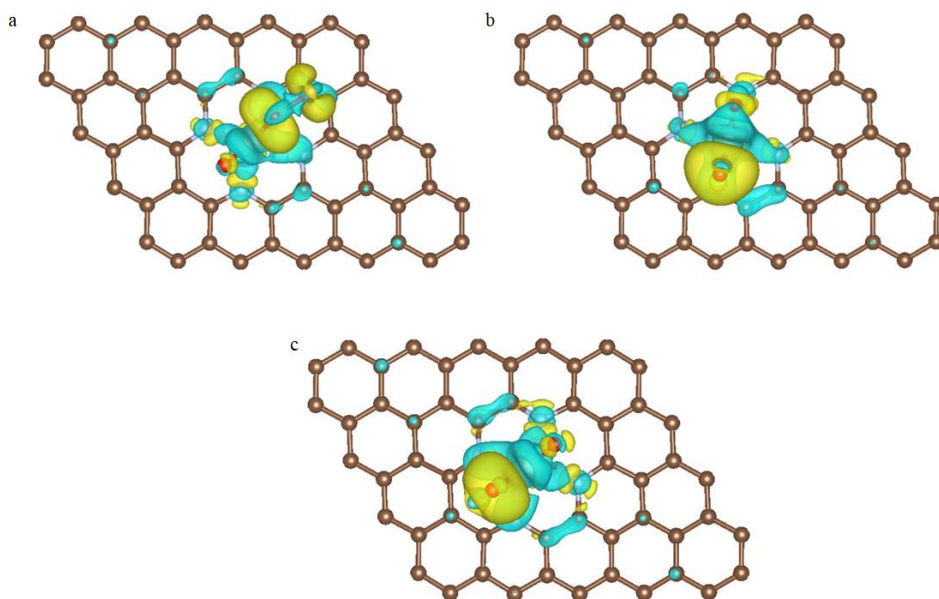
Figure S6. The charge redistribution of the HfN$_4$O moiety adsorbing intermediate species. (a) The charge redistribution induced by *OOH adsorption on the HfN$_4$O moiety. (b) The charge redistribution induced by *O adsorption on the HfN$_4$O moiety. (c) The charge redistribution induced by *OH adsorption on the HfN$_4$O moiety.
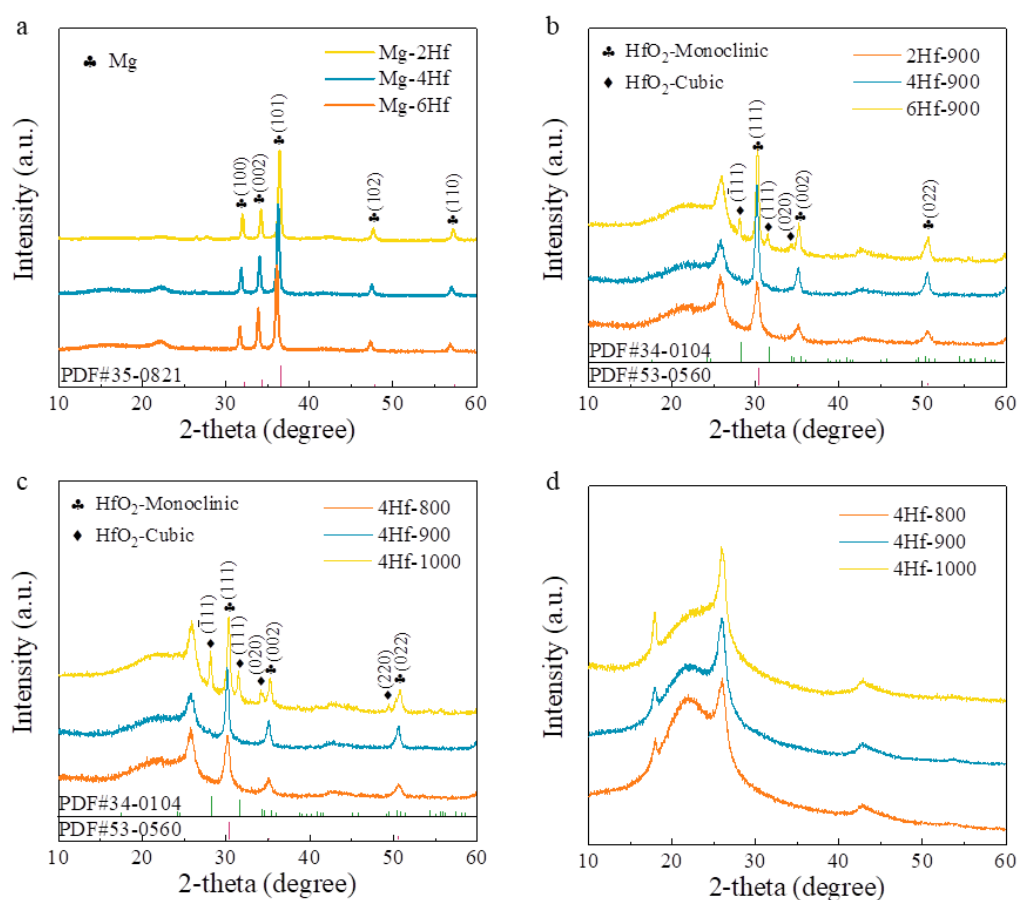
Figure S7. Phase compositions. (a) XRD patterns of Mg-2Hf, Mg-4Hf, and Mg-6Hf samples after ball-malling treatment. (b) XRD patterns of Mg-2Hf, Mg-4Hf, and Mg-6Hf samples, respectively. The samples were pyrolyzed at 900 ℃ under a mixing condition of CO_2/NH_3. (c) XRD patterns of Mg-4Hf samples pyrolyzed at 800, 900 and 1000 ℃ under CO_2/NH_3 atmosphere, respectively. (d) XRD patterns of Mg-4Hf samples pyrolyzed at 800, 900 and 1000 ℃ a mixing condition of CO_2/NH_3 following by picking, respectively. The strong peaks observed at about 18° and 25° can be attributed to the presence of nitrogen-doped carbon within the catalysts[7].

Figure S8. Digital photos of s-Hf-N/O-C catalyst synthesized by a two-step technique.
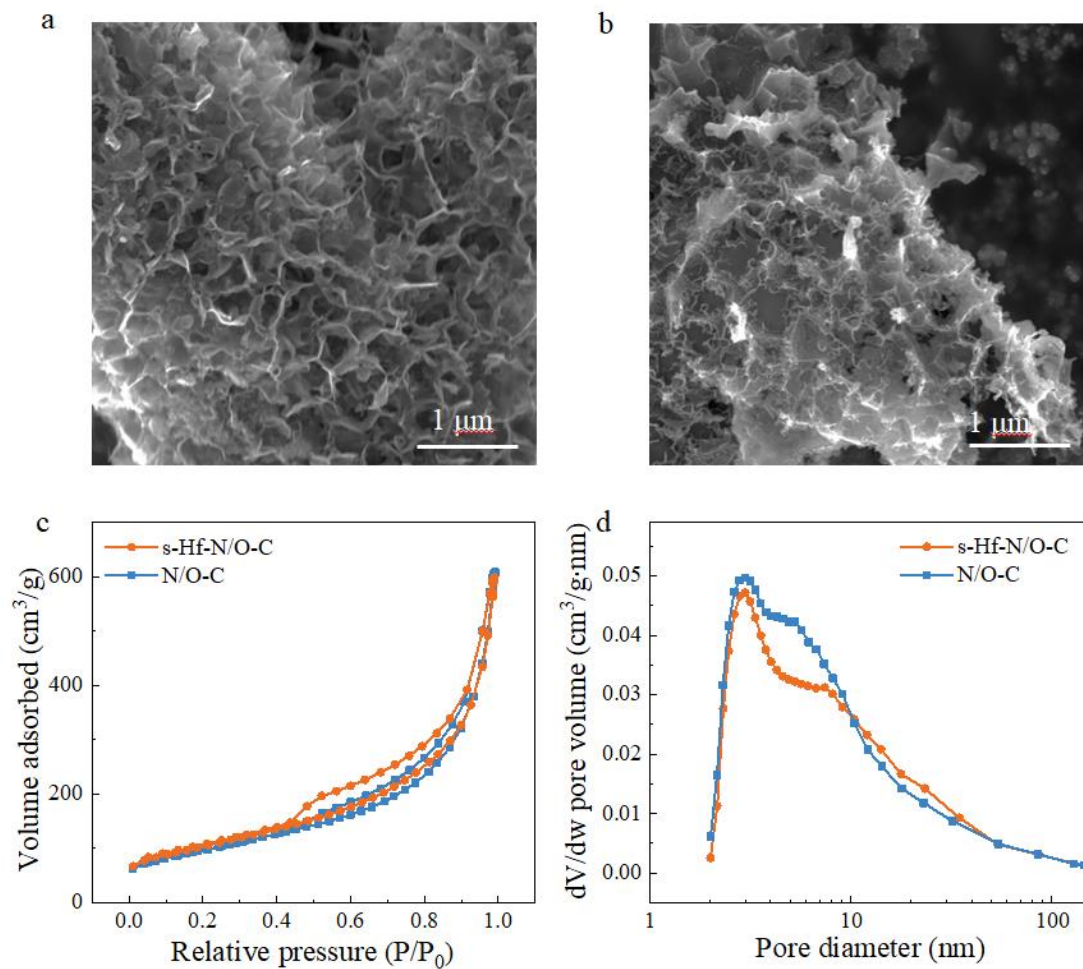
Figure S9. Microstructural charactristics. (a, b) The overall SEM morphologies of s-Hf-N/O-C and N/O-C. (c, d) N_2 adsorption/desorption plots and pore distribution of s-Hf-N/O-C and N/O-C.
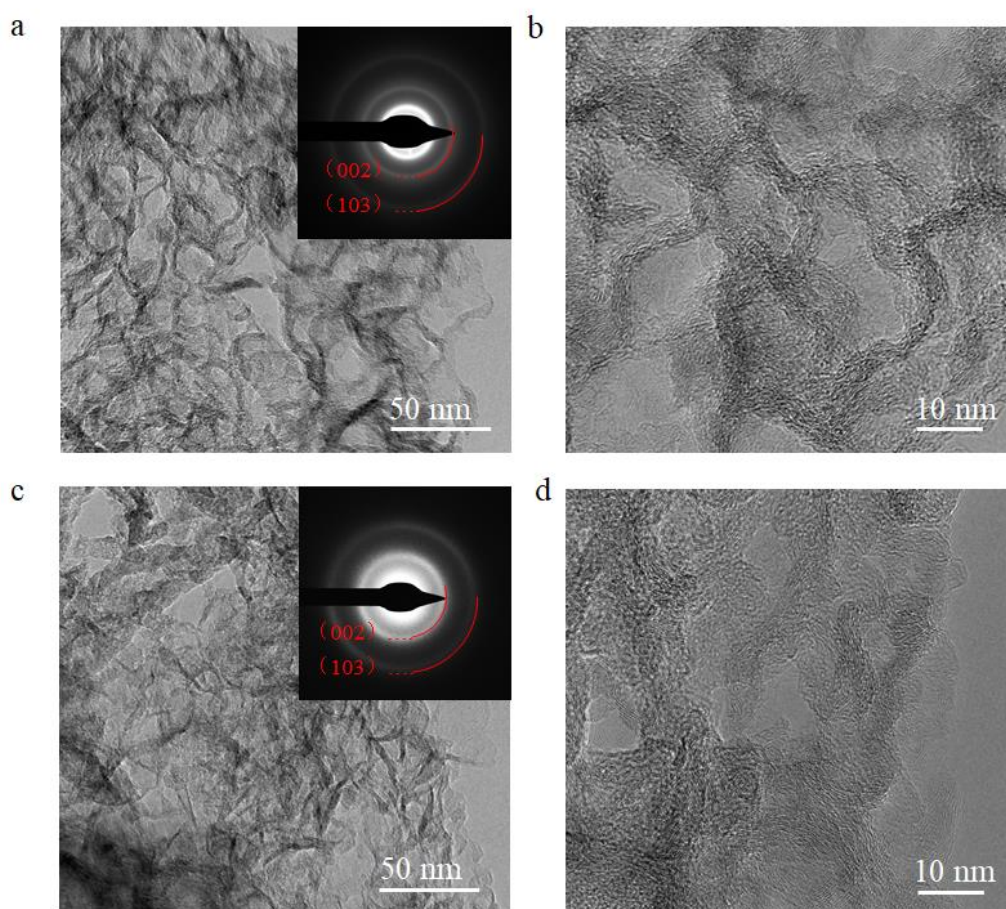
Figure S10. TEM and HRTEM images. (a, b) s-Hf-N/O-C. (c, d) N/O-C. The two catalysts had similar microstructure, in which no nanoparticles were observed. The inset were selected area electron diffraction (SAED) pattern of the s-Hf-N/O-C and N/O-C, which exhibited the poor crystallinity of carbon frame. No other diffraction rings were observed, confirming the absence of other crystalline or amorphous materials within the catalyst.
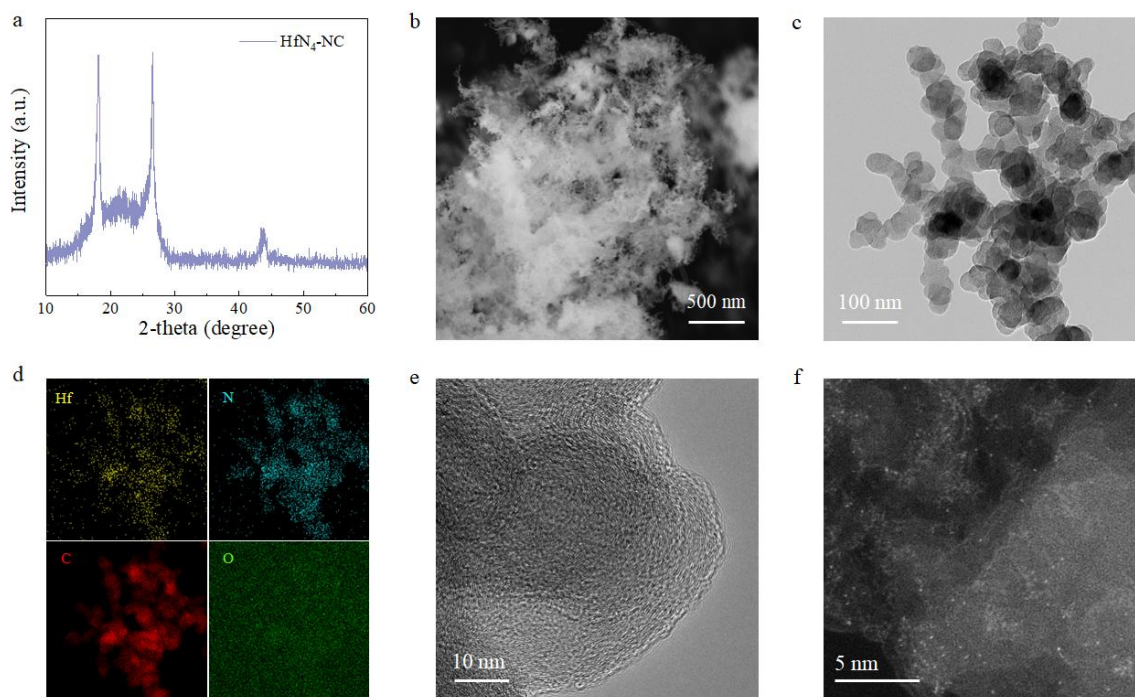
Figure S11. The structural characteristics of the s-Hf-N-C. (a) XRD patterns. (b) SEM images. (c) TEM images. (d) EDS elemental mapping. (e) HRTEM images. (f) AC-HAADF-STEM image.
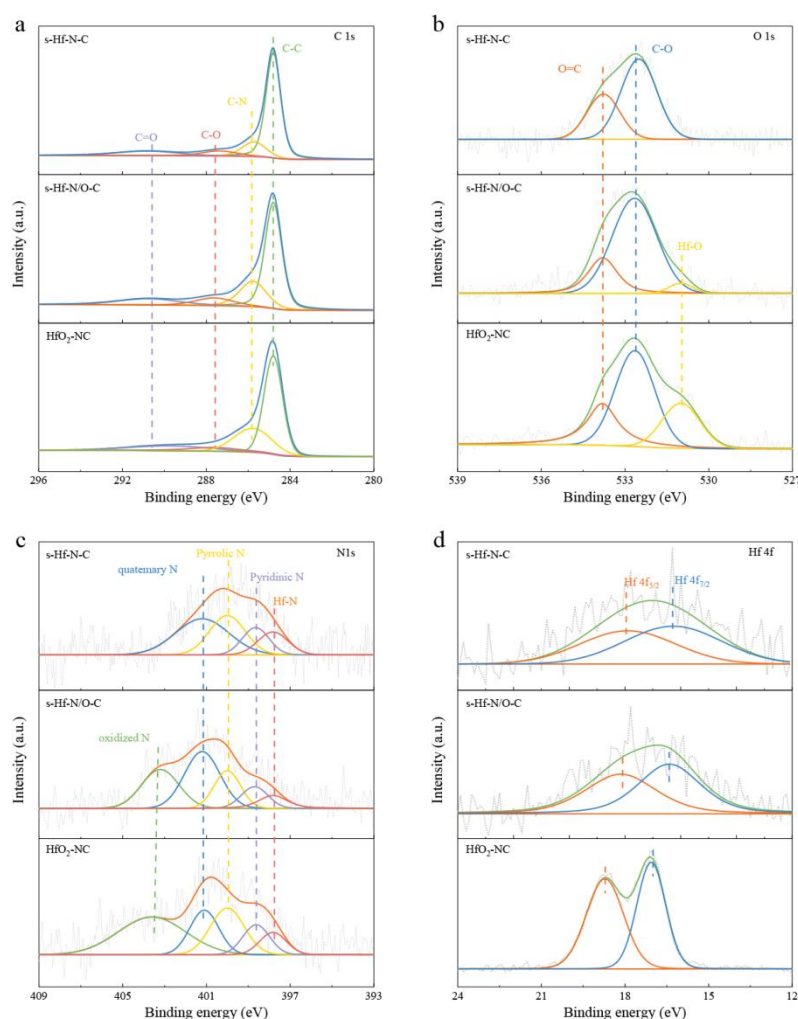
Figure S12. XPS spectroscopy of s-Hf-N-C, s-Hf-N/O-C, and HfO$_2$-N-C. (a-d) High-resolution XPS spectra of C1s, O 1s, N 1s and Hf 4f. In the high-resolution C 1s spectra, no significant differences are observed among the three samples. In the high-resolution O 1s spectra, it is found that there was no discernible presence of Hf-O bonds in the s-Hf-N-C sample, compared to the pronounced Hf-O coordination peak in the HfO$_2$-N-C. Only a small amount of Hf-O bonds are detected in the s-Hf-N/O-C. High-resolution N 1s spectra shows the presence of Hf-N bonds in all three samples. However, the presence of oxidized N is observed in both the HfO$_2$-N-C and s-Hf-N/O-C samples due to the presence of O atoms. In the high-resolution Hf 4f spectra, the HfO$_2$-N-C exhibits distinct HfO$_2$ double peaks at 17.06 eV and 18.72 eV, respectively, and the s-Hf-N-C and s-Hf-N/O-C samples display broad

single peaks with a noticeable redshift, indicating a significantly different Hf coordination environment in contrast to HfO_2 particles.
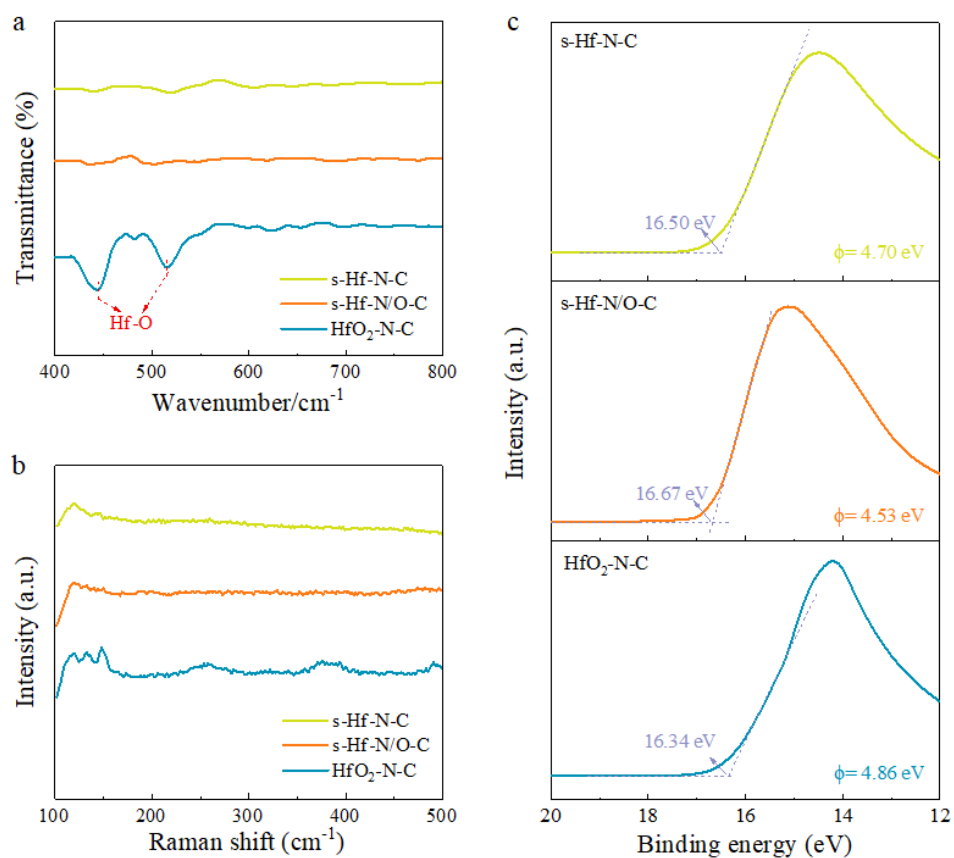
Figure S13. Spectral analysis of the s-Hf-N-C, s-Hf-N/O-C and HfO_2-N-C. (a) FT-IR spectra (b) Raman spectra. (c) Ultraviolet photoelectron spectra (UPS).
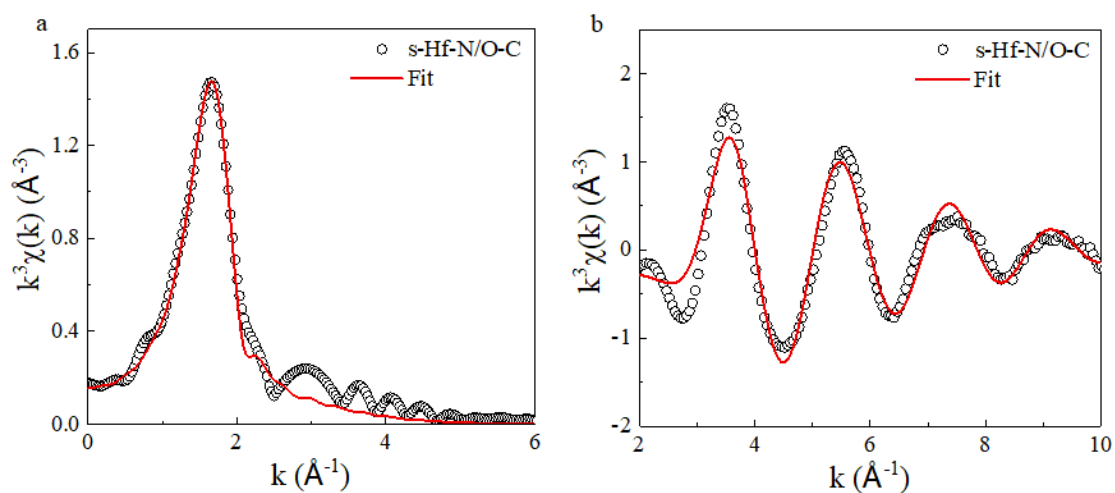
Figure S14. XAFS analyses. (a) FT-EXAFS fitting curves of the s-Hf-N/O-C. The best-fit structural parameters are listed in Table S6, Supporting Information. (b) The corresponding EXAFS k-space fitting results of the s-Hf-N/O-C.
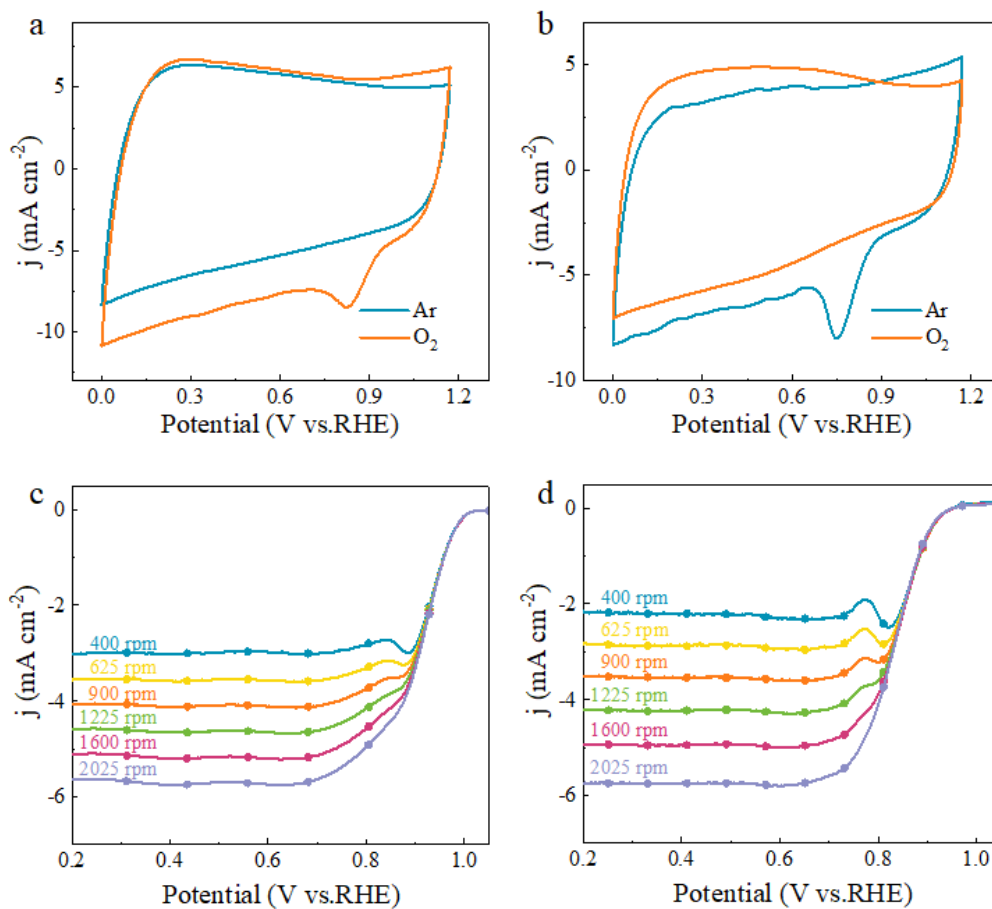
Figure S15. Electrochemical tests. (a-b) CV curves of the s-Hf-N/O-C, s-Hf-N-C in an 0.1 M KOH solution within a potential range from 0 to 1.2 V (scan rate: 50 mV s^{-1}). (c-d) LSV curves of the s-Hf-N/O-C and s-Hf-N-C with different rotation rates during the RDE test.
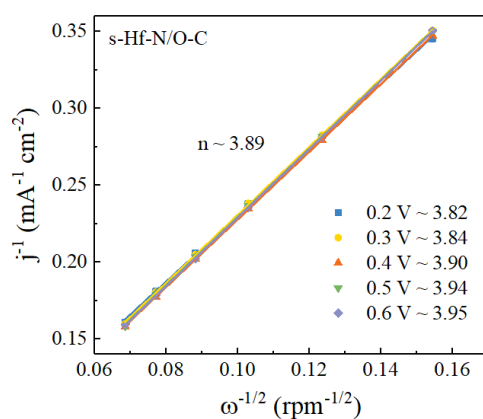
Figure S16. Koutecky-Levich plots of s-Hf-N/O-C with a sweep rate of 5 mV s^{-1} (n ≈ 3.89).
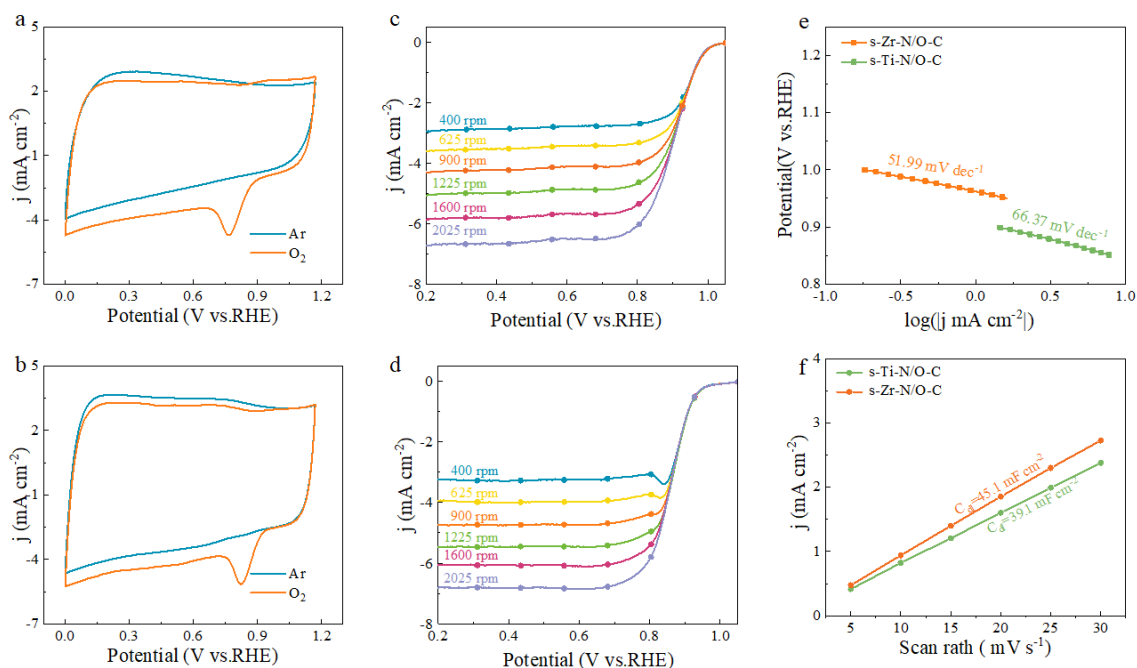
Figure S17. Electrochemical tests. (a, b) CV curves of the s-Ti-N/O-C, and s-Zr-N/O-C in a 0.1 M KOH solution within a potential range from 0 to 1.2 V (scan rate: 50 mV s^{-1}). (c, d) LSV curves of the s-Ti-N/O-C, and s-Zr-N/O-C with different rotation rates during the RDE test. (e) Tafel plots of the s-Zr-N/O-C and s-Ti-N/O-C in 0.1 M KOH. (f) Fitting results of double layer capacity (C$_{dl}$) of the s-Zr-N/O-C and s-Ti-N/O-C.
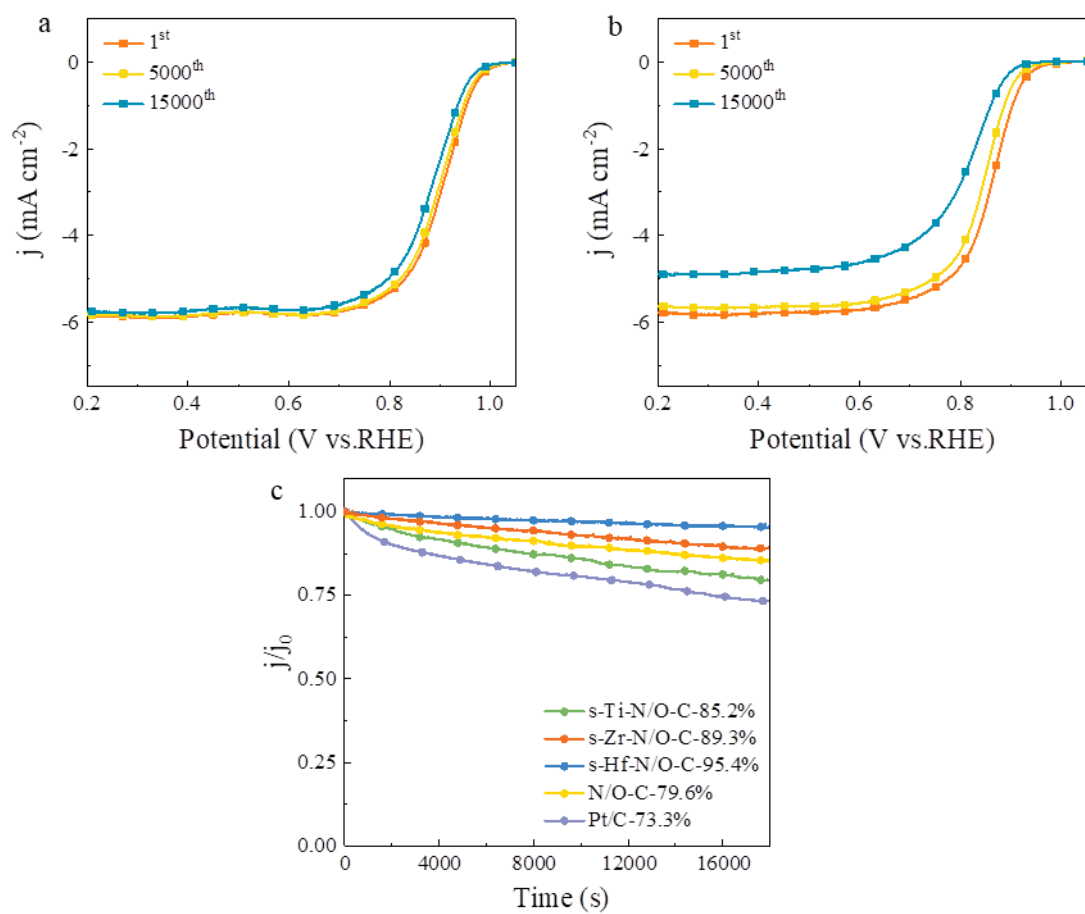
Figure S18. (a, b) Electrochemical stability of s-Zr-N/O-C, and s-Ti-N/O-C, respectively. (c) Chronoamperometry (CA) test of the catalysts at 0.6 V with 1,600 rpm in a O_2-saturated 0.1 M KOH solution.
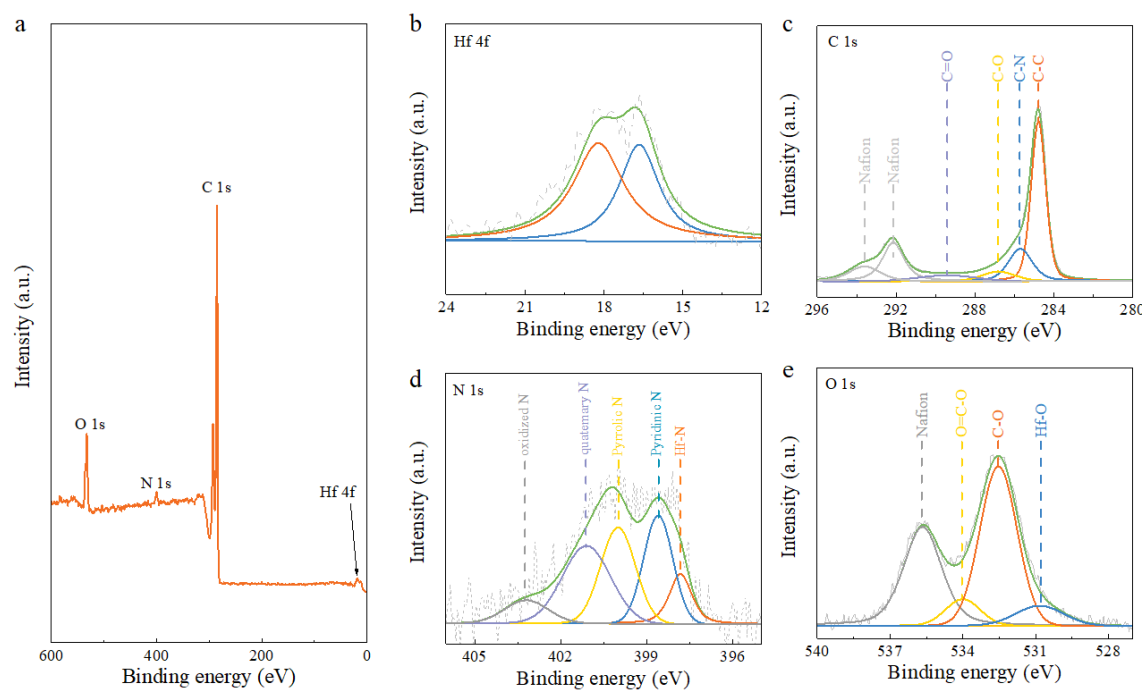
Figure S19. XPS spectroscopy of s-Hf-N/O-C after 15000 cycles in a 0.1 M KOH solution. (a) XPS survey spectrum, suggesting the existence of Hf, N, O, and C elements in the s-Hf-N/O-C. (b) High-resolution XPS spectra of Hf 4f. (c) High-resolution XPS spectra of C 1s. (d) High-resolution XPS spectra of N 1s. (e) High-resolution XPS spectra of O 1s.
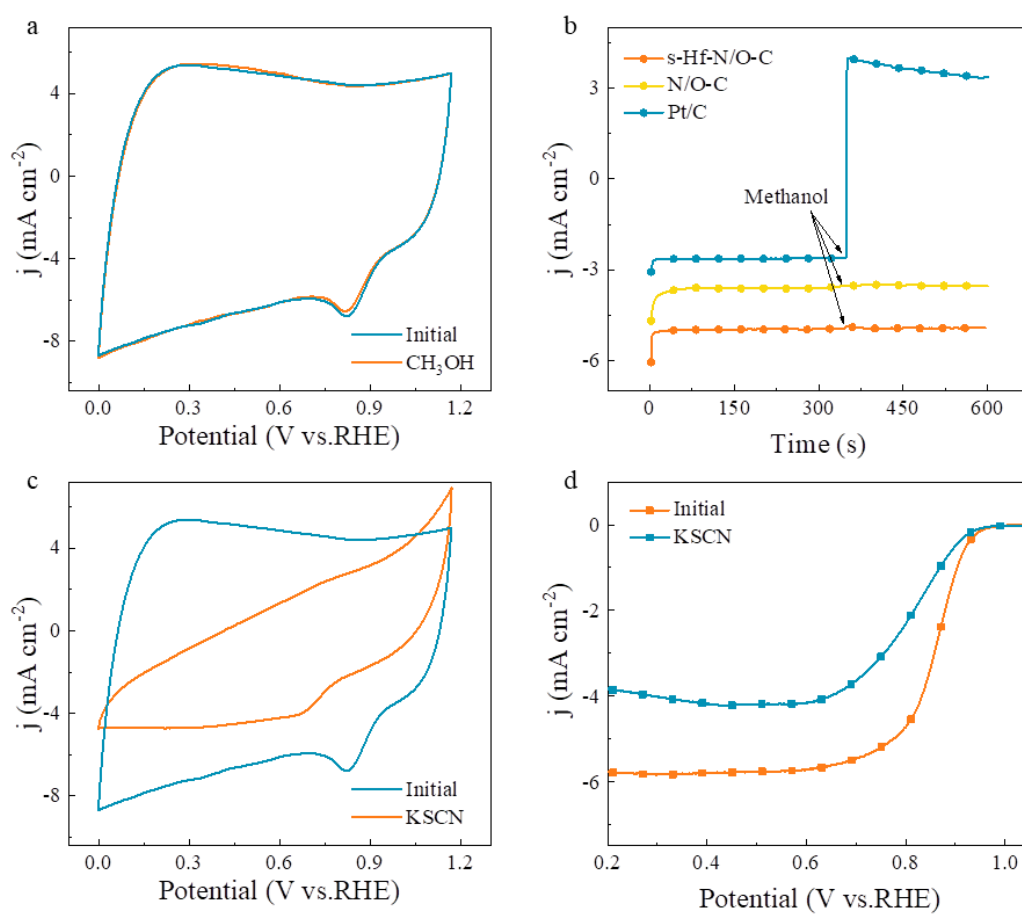
Figure S20. Toxicity resistance test. The measurements were carried out by adding CH₃OH (0.01 M) into the solution. (a) CV. (b) CA. The measurements were carried out by adding KSCN (0.01 M) into the solution. (c) CV. (d) LSV.

Table S1. Calculated bond length of MN_4 and MN_4O (M = Ti, Zr, Hf).

	M-N1	M-N2	M-N3	M-N4	M-O
TiN_4	2.071	1.986	2.071	1.986	/
TiN_4O	2.079	2.077	2.079	2.077	2.136
ZrN_4	2.087	2.001	2.087	2.001	/
ZrN_4O	2.096	2.092	2.096	2.092	2.154
HfN_4	2.114	2.093	2.114	2.093	/
HfN_4O	2.174	2.174	2.174	2.174	2.223

Table S2. Metal concentration in the different samples determined by inductively coupled plasma mass spectrometry (ICP-MS).

Sample	Metal concentration (wt.%)
s-Hf-N/O-C	5.08 (Hf)
s-Zr-N/O-C	3.99 (Zr)
s-Ti-N/O-C	4.35 (Ti)

Table S3. Chemical composition of the s-Hf-N-C recorded by XPS.

Elements	Content (at.%)	Assignment	Position (eV)	Content (at.%)
C	93.82	C-C	284.80	65.87
		C-N	285.72	16.57
		C-O	287.36	8.64
		C=O	289.81	8.92
N	3.13	Hf-N	397.82	293
		Pyridinic N	398.65	307
		Pyrrolic N	400.00	592
		Graphitic N	401.20	815
O	2.85	C-O	532.50	1824
		O=C-O	533.77	938
Hf	0.2	Hf 4f$_{7/2}$	18.35	52.71
		Hf 4f$_{5/2}$	20.10	47.29

Table S4. Chemical composition of the s-Hf-N/O-C recorded by XPS.

Elements	Content (at.%)	Assignment	Position (eV)	Content (at.%)
C	91.52	C-C	284.80	57.19
		C-N	285.77	21.61
		C-O	287.61	9.39
		C=O	290.75	11.81
N	3.70	Hf-N	397.82	8.73
		Pyridinic N	398.62	11.75
		Pyrrolic N	400.00	23.21
		Graphitic N	401.10	18.86
		Oxidized N	403.60	37.45
O	4.51	Hf-O	530.99	4.10
		C-O	532.66	73.66
		O=C-O	533.80	22.24
Hf	0.27	Hf 4f$_{7/2}$	18.05	52.74
		Hf 4f$_{5/2}$	19.80	47.26

Table S5. Chemical composition of the HfO$_2$-N-C recorded by XPS.

Elements	Content (at.%)	Assignment	Position (eV)	Content (at.%)
C	89.85	C-C	284.80	59.85
		C-N	285.77	19.34
		C-O	287.6	9.24
		C=O	289.75	11.57
N	3.10	Hf-N	397.82	8.12
		Pyridinic N	398.70	10.48
		Pyrrolic N	400.00	18.08
		Graphitic N	401.20	36.89
		Oxidized N	403.20	34.55
O	6.62	Hf-O	530.99	23.16
		C-O	532.64	50.99
		O=C-O	533.81	25.85
Hf	0.43	Hf 4f$_{7/2}$	16.85	57.11
		Hf 4f$_{5/2}$	18.60	42.89

Table S6. EXAFS fitting parameters at the Hf L-edge for various samples ($S_0{}^2 = 0.94$).

Sample	Shell	CN^a	$R(\text{Å})^b$	σ^2 ($\text{Å}^2 \cdot 10^{-3}$) ^{c}	$\Delta E_0(\text{eV})^d$	R factor
			Hf L3-edge			
HfO$_2$	Hf-O	6*	2.13±0.01	0.0085	5.41±1.31	1.4%
Hf	Hf-Hf	12*	3.06±0.04	0.0022	1.09±3.08	1.2%
s-Hf-N-C	Hf-N	4.4±0.2	2.10±0.04	0.0051	4.49±2.62	1.0%
s-Hf-N/O-C	Hf-N	4.0±0.2	2.02±0.03	0.0088	4.37±2.52	1.7%
	Hf-O	1.1±0.2	2.14±0.02			

Table S7. Comparison of ORR performance between the s-Hf-N/O-C and other non-precious catalysts reported in the literatures under O_2-saturated 0.1 M KOH solutions.

	Eletrocatalytst	$E_{(onset)}$ (V vs.RHE)	$E_{(1/2)}$ (V vs.RHE)	Ref.
1	s-Hf-N/O-C	1.050	0.920	This work
2	s-Zr-N/O-C	0.983	0.905	This work
3	s-Ti-N/O-C	0.937	0.865	This work
4	Co$_2$/Fe-N@CHC	1.000	0.915	[8]
5	O-Zr-N-C	0.982	0.910	[9]
6	Mg-N-C	1.030	0.910	[10]
7	Fe/Zn-N-C	0.980	0.906	[11]
8	Ca-N,O/C	0.980	0.900	[12]
9	Fe$_{SA}$-N-C	0.965	0.900	[13]
10	Zn-B/N-C	0.960	0.886	[14]
11	Co@DMOF-900	0.930	0.866	[15]
12	Fe SA-NSC-900	0.940	0.86	[16]
13	YN$_4$-Cl-2	0.910	0.850	[17]

Table S8. Hf contents after CV cycling determined by ICP-MS.

Sample	Hf concentration
Electrolyte (KOH)	**0 (μg/L)**
s-Hf-N/O-C (Titanium mesh)	**5.01 (wt.%)**

Table S9. Chemical composition after CV cycling of the s-Hf-N/O-C recorded by XPS.

Elements	Assignment	Position (eV)	Content (at.%)
C	C-C	284.80	44.54
	C-N	285.70	15.66
	C-O	286.80	5.92
	C=O	289.40	5.93
	Nafion	292.15	18.76
	Nafion	293.6	9.19
N	Hf-N	397.82	7.88
	Pyridinic N	398.60	29.50
	Pyrrolic N	400.00	26.41
	Graphitic N	401.10	25.06
	Oxidized N	403.20	11.15
O	Hf-O	530.30	7.88
	C-O	532.35	48.59
	O=C-O	534.02	7.49
	Nafion	535.66	36.04
Hf	Hf 4f$_{7/2}$	17.65	52.23
	Hf 4f$_{5/2}$	19.40	47.77

References

[1]   a)G. Kresse, J. Hafner, *Phys. Rev. B* **1993**, 47, 558; b)P. E. Blöchl, *Phys. Rev. B* **1994**, 50, 17953.

[2]   J. P. Perdew, K. Burke, M. Ernzerhof, *Phys. Rev. Lett.* **1996**, 77, 3865.

[3]   E. Jung, H. Shin, B.-H. Lee, V. Efremov, S. Lee, H. S. Lee, J. Kim, W. Hooch Antink, S. Park, K.-S. Lee, *Nat. Mater.* **2020**, 19, 436.

[4]   L. Han, H. Cheng, W. Liu, H. Li, P. Ou, R. Lin, H.-T. Wang, C.-W. Pao, A. R. Head, C.-H. Wang, *Nat. Mater.* **2022**, 21, 681.

[5]   B. Ravel, M. Newville, *J. Synchrotron Radiat.* **2005**, 12, 537.

[6]   R. Gao, J. Wang, Z.-F. Huang, R. Zhang, W. Wang, L. Pan, J. Zhang, W. Zhu, X. Zhang, C. Shi, *Nat. Energy* **2021**, 6, 614.

[7]   a)C. Zhao, Y. Zhang, Y. Jia, B. Li, W. Tang, C. Shang, R. Mo, P. Li, S. Liu, S. Zhang, *Nat. Commun.* **2023**, 14, 1112; b)X. Xiao, Y. Gao, L. Zhang, J. Zhang, Q. Zhang, Q. Li, H. Bao, J. Zhou, S. Miao, N. Chen, *Adv. Mater.* **2020**, 32, 2003082.

[8]   Z. Wang, X. Jin, C. Zhu, Y. Liu, H. Tan, R. Ku, Y. Zhang, L. Zhou, Z. Liu, S. J. Hwang, *Adv. Mater.* **2021**, 33, 2104718.

[9]   X. Wang, Y. An, L. Liu, L. Fang, Y. Liu, J. Zhang, H. Qi, T. Heine, T. Li, A. Kuc, *Angew. Chem. Int. Ed.* **2022**, 134, e202209746.

[10]   S. Liu, Z. Li, C. Wang, W. Tao, M. Huang, M. Zuo, Y. Yang, K. Yang, L. Zhang, S. Chen, *Nat. Commun.* **2020**, 11, 938.

[11]   H. Li, S. Di, P. Niu, S. Wang, J. Wang, L. Li, *Energy Environ. Sci.* **2022**, 15, 1601.

[12]   Z. Lin, H. Huang, L. Cheng, W. Hu, P. Xu, Y. Yang, J. Li, F. Gao, K. Yang, S. Liu, *Adv. Mater.* **2021**, 33, 2107103.

[13]   L. Jiao, R. Zhang, G. Wan, W. Yang, X. Wan, H. Zhou, J. Shui, S.-H. Yu, H.-L. Jiang, *Nat. Commun.* **2020**, 11, 2831.

[14]   J. Wang, H. Li, S. Liu, Y. Hu, J. Zhang, M. Xia, Y. Hou, J. Tse, J. Zhang, Y. Zhao, *Angew. Chem.* **2021**, 133, 183.

[15]   S. Yuan, J. Zhang, L. Hu, J. Li, S. Li, Y. Gao, Q. Zhang, L. Gu, W. Yang, X. Feng, *Angew. Chem. Int. Ed.* **2021**, 60, 21685.

[16]   M. Wang, W. Yang, X. Li, Y. Xu, L. Zheng, C. Su, B. Liu, *ACS Energy Lett.* **2021**, 6, 379.

[17]   B. Ji, J. Gou, Y. Zheng, X. Pu, Y. Wang, P. Kidkhunthod, Y. Tang, *Adv. Mater.* **2023**, 2300381.